

FACULTY
OF MATHEMATICS
AND PHYSICS
Charles University

1

BACHELOR THESIS

2

Martin Vavřík

3

**Simulation and Reconstruction
of Charged Particle Trajectories
in an Atypic Time Projection Chamber**

4

5

Institute of Particle and Nuclear Physics

6

Supervisor of the bachelor thesis: Mgr. Tomáš Sýkora, Ph.D.

7

Study programme: Physics

8

Prague 2025

- ⁹ I declare that I carried out this bachelor thesis independently, and only with the
¹⁰ cited sources, literature and other professional sources. It has not been used to
¹¹ obtain another or the same degree.
- ¹² I understand that my work relates to the rights and obligations under the Act
¹³ No. 121/2000 Sb., the Copyright Act, as amended, in particular the fact that the
¹⁴ Charles University has the right to conclude a license agreement on the use of this
¹⁵ work as a school work pursuant to Section 60 subsection 1 of the Copyright Act.

In date
Author's signature

Title: Simulation and Reconstruction of Charged Particle Trajectories in an Atypical Time Projection Chamber *Added hyphen to avoid overfull hbox*

Author: Martin Vavřík

Institute: Institute of Particle and Nuclear Physics

Supervisor: Mgr. Tomáš Sýkora, Ph.D., Institute of Particle and Nuclear Physics

Abstract: Abstract.

Keywords: key words

¹⁷ Contents

| | | |
|---------------|--|-----------|
| ¹⁸ | Motivation | 3 |
| ¹⁹ | 0.1 ATOMKI Anomaly | 3 |
| ²⁰ | 0.1.1 ATOMKI Measurements | 3 |
| ²¹ | 0.1.2 Other Experiments | 4 |
| ²² | 0.2 X17 Project at IEAP CTU | 6 |
| ²³ | 1 Time Projection Chamber | 9 |
| ²⁴ | 1.1 Charge transport in gases | 9 |
| ²⁵ | 1.1.1 Drift | 9 |
| ²⁶ | 1.1.2 Diffusion | 10 |
| ²⁷ | 1.2 Readout | 11 |
| ²⁸ | 1.2.1 Multi-Wire Proportional Chamber | 11 |
| ²⁹ | 1.2.2 Gas Electron Multiplier | 11 |
| ³⁰ | 1.2.3 Micromegas | 12 |
| ³¹ | 1.2.4 Parallel Plate Chamber | 12 |
| ³² | 1.3 Orthogonal Fields TPC at IEAP CTU | 12 |
| ³³ | 1.3.1 Motivation and Associated Challenges | 12 |
| ³⁴ | 1.3.2 Coordinate Systems and Dimensions | 13 |
| ³⁵ | 1.3.3 Magnetic Field Simulation | 15 |
| ³⁶ | 2 Track Simulation | 18 |
| ³⁷ | 2.1 Microscopic Simulation | 18 |
| ³⁸ | 2.2 Runge-Kutta Simulation | 19 |
| ³⁹ | 3 Track Reconstruction | 22 |
| ⁴⁰ | 3.1 Reconstruction Assuming Steady Drift | 22 |
| ⁴¹ | 3.2 Ionization Electron Map | 24 |
| ⁴² | 3.2.1 Gradient Descent Search | 27 |
| ⁴³ | 3.2.2 Interpolation on the Inverse Grid | 28 |
| ⁴⁴ | 3.3 Discrete Reconstruction | 29 |
| ⁴⁵ | 4 Energy Reconstruction | 31 |
| ⁴⁶ | 4.1 Cubic Spline Fit | 31 |
| ⁴⁷ | 4.2 Circle and Lines Fit | 33 |
| ⁴⁸ | 4.2.1 Two-dimensional fit | 33 |
| ⁴⁹ | 4.2.2 Three-dimensional fit | 35 |
| ⁵⁰ | 4.3 Runge-Kutta Fit | 38 |
| ⁵¹ | Conclusion | 41 |
| ⁵² | Bibliography | 44 |
| ⁵³ | List of Figures | 48 |
| ⁵⁴ | List of Tables | 50 |

56 Motivation

57 A Time Projection Chamber (TPC) [refs] is a type of gaseous detector that detects
58 charged particle trajectories by measuring the positions and drift time of ions cre-
59 ated in the gas. The energies of these particles can be inferred from the curvatures
60 of their trajectories in the magnetic field (specific field inside the TPC).

61 The goal of this thesis is to develop an algorithm for the reconstruction of
62 charged particle trajectories and energy in an *atypic* TPC with orthogonal elec-
63 tric and magnetic fields, hereafter referred to as the Orthogonal Fields TPC
64 (OFTPC), used in the X17 project at the Institute of Experimental and Applied
65 Physics, Czech Technical University in Prague (IEAP CTU). Furthermore, we
66 present the results of testing of several (gradually improving) developed algo-
67 rithms with different samples of simulated data. Put this somewhere, (maybe
68 just the abstract?). We use the Garfield++ toolkit [1] for simulations in combina-
69 tion with the ROOT framework [2] for data analysis and visualization. Some of
70 our more demanding simulations are run on the MetaCentrum grid [3].

71 The X17 project in IEAP CTU aims to reproduce measurements of anomalous
72 behavior in the angular correlation distribution of pairs produced by the Internal
73 Pair Creation (IPC) mechanism [4] during the decay of certain excited nuclei
74 (${}^8\text{Be}$, ${}^{12}\text{C}$, and ${}^4\text{He}$) observed by a team at ATOMKI in Hungary. I would leave
75 this here as a short summary before I explain it in more detail in the sections
76 below.

77 Add citations: X17 project, VdG. Maybe also TPC, etc.

78 0.1 ATOMKI Anomaly

79 Many different theories propose the existence of *new light bosons* that are weakly
80 coupled to ordinary matter [5]. These particles are potential dark matter candi-
81 dates and could solve other issues with the Standard Model, such as the strong
82 CP problem and the anomalous muon magnetic moment.

83 A possible way of detecting such bosons with a short lifetime is to observe
84 nuclear transitions of excited nuclei. If a boson was emitted during the transition
85 and subsequently decayed into an electron-positron pair, we could observe this
86 as a peak on top of the standard e^+e^- angular correlation from the Internal Pair
87 Creation (IPC) and the External Pair Creation (EPC).

88 0.1.1 ATOMKI Measurements

89 Historically, there were several measurements of the IPC in nuclear transitions
90 in ${}^8\text{Be}$ at Institute für Kernphysik (Frankfurt) [6, 7, 8] and at ATOMKI [9, 10]
91 resulting in different anomalies with invariant mass in the range 5–15 MeV. This
92 prompted a development of a better spectrometer at ATOMKI.

93 In 2015, a group at ATOMKI led by Attila Krasznahorkay observed an anom-
94 arious IPC in ${}^8\text{Be}$ [11]. They used the ${}^7\text{Li}(p, \gamma){}^8\text{Be}$ reaction at the $E_p = 1030$ keV
95 proton capture resonance to prepare the 18.15 MeV excited state ($J^\pi = 1^+, T =$
96 = 0). This state decays predominantly through M1 transitions to the ground
97 state ($J^\pi = 0^+, T = 0$) and to the 3.03 MeV state ($J^\pi = 2^+, T = 0$) [12].

98 The angular correlation of the e^+e^- pairs created internally in these transitions
99 were measured and compared to the simulation; results from a narrow $E_{\text{sum}} =$
100 $= 18$ MeV region are shown in Figure 0.1a. The simulation includes boson decay
101 pairs for different boson masses. The disparity parameter y is defined as

$$y = \frac{E_{e^-} - E_{e^+}}{E_{e^-} + E_{e^+}}, \quad (0.1)$$

102 where E_{e^-} and E_{e^+} are the kinetic energies of the electron and positron.

103 Their experimental setup was later upgraded ([details?](#)) and used for new mea-
104 surements. In 2022 the ${}^8\text{Be}$ anomaly was also measured using the $E_p = 441$ keV
105 resonance to produce the 17.64 MeV excited state ($J^\pi = 1^+$, $T = 1$) which again
106 decays primarily to the ground state and the 3.03 MeV state [12]. The anomaly
107 was also measured for $E_p = 650$ and 800 keV where E1 transitions from the direct
108 proton capture dominate [13]. The results for e^+e^- with $E_{\text{sum}} \in [13.5, 20]$ MeV
109 are shown in Figure 0.1b.

110 The newer setup was also used in 2021 to study the ${}^3\text{H}(p, e^+e^-){}^4\text{He}$ reaction at
111 $E_p = 510, 610$ and 900 keV [14], inducing direct and resonant capture populating
112 the overlapping first 20.21 MeV ($J^\pi = 0^+$) and second 21.01 MeV ($J^\pi = 0^-$)
113 excited states [15]. The comparison of simulated and measured e^+e^- pair angular
114 correlations in the $E_{\text{sum}} \in [18, 22]$ MeV region is shown in Figure 0.1c.

115 In 2022, another anomaly was measured in the ${}^{11}\text{B}(p, e^+e^-){}^{12}\text{C}$ process [16].
116 The $E_p = 1388$ keV resonance was used to populate the 17.23 MeV excited state
117 ($J^\pi = 1^-, T = 1$) with a large width $\Gamma = 1.15$ MeV [17]. This state decays
118 mainly through E1 transitions to the ground state $J^\pi = 0^+$ and to the 4.44 MeV
119 state $J^\pi = 2^+$. To compensate for energy losses in the target, five energies in
120 the range $E_p = 1.5\text{--}2.5$ MeV were used. The experimental angular correlation for
121 the 17.23 MeV transition to the ground state is shown in Figure 0.1d.

122 Possible explanations of the anomaly include experimental effects, higher or-
123 der processes in the Standard Model [18, 19] or even a protophobic fifth force
124 mediated by a new 17 MeV boson X17 [20]. [Zhang and Miller: <https://www.sciencedirect.com/science/article/pii/S0370269321000010>](https://www.sciencedirect.com/science/article/pii/S0370269321000010)

126 0.1.2 Other Experiments

127 Since the ATOMKI measurements, several experiments have been initiated to
128 attempt to replicate the results and search for the hypothetical X17 particle.
129 [Here are a few with results. Could cite the ATOMKI review paper here.](#)

130 Two-arm e^+e^- spectrometer in Hanoi

131 The anomaly in ${}^8\text{Be}$ has been observed with $> 4\sigma$ confidence by a team at the
132 Hanoi University of Sciences for $E_p = 1225$ keV [21]. They built a two-arm
133 spectrometer in collaboration with ATOMKI and calibrated it using the 17.6 MeV
134 M1 transition. The results are shown in Figure 0.2.

135 Collisions at Nuclotron in Dubna

136 At the Joint Institute for Nuclear Research in Dubna, signal in the form of en-
137 hanced structures in the $\gamma\gamma$ spectra at ~ 17 and ~ 38 MeV invariant masses

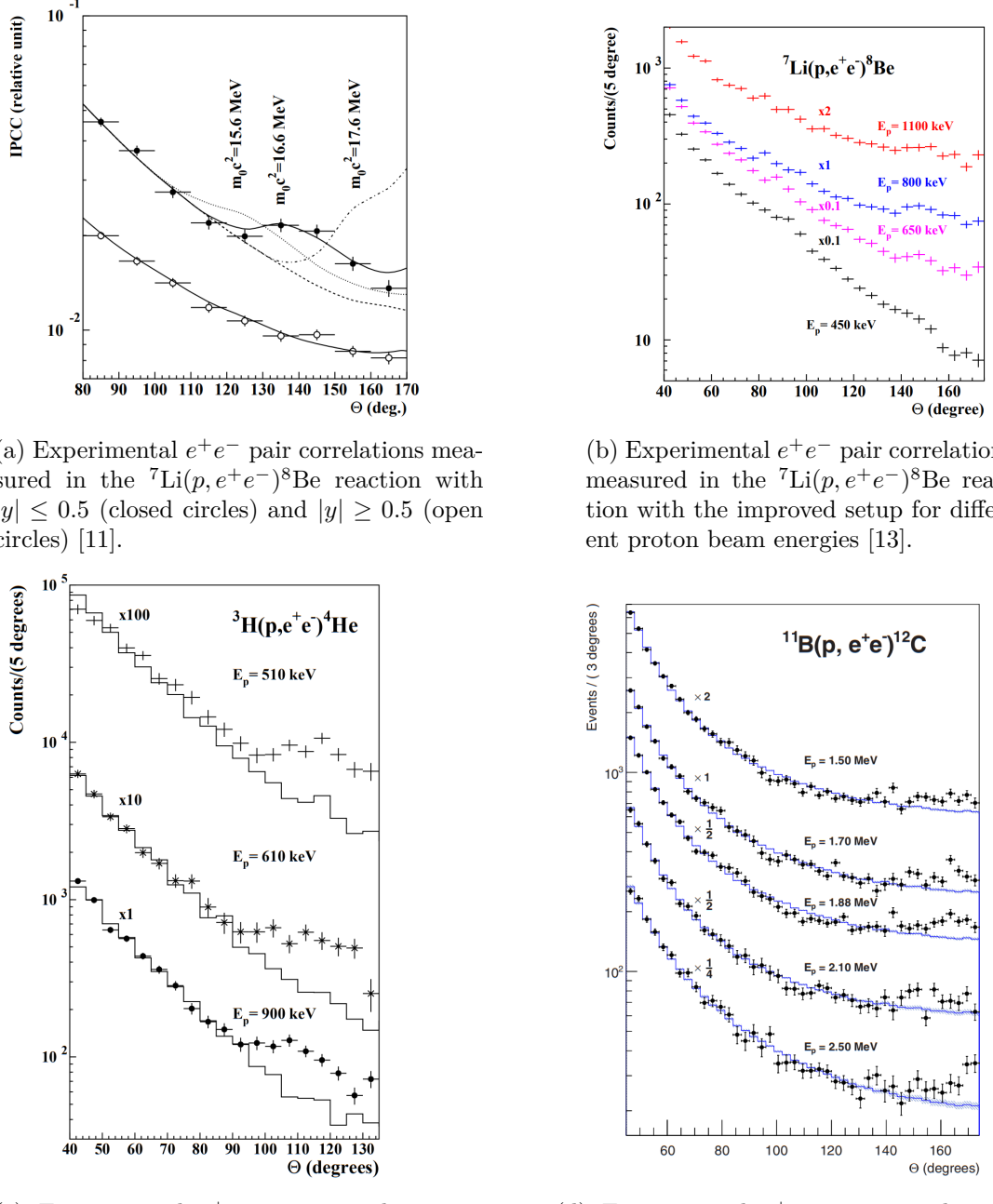


Figure 0.1: The ATOMKI anomalous IPC measured for different nuclei.



Figure 0.2: Results from the Hanoi spectrometer – angular e^+e^- pair correlations measured in the ${}^7\text{Li}(p, e^+e^-){}^8\text{Be}$ reaction at $E_p = 1225$ keV [21].

for $p + \text{C}$, $d + \text{C}$ and $d + \text{Cu}$ reactions at momenta 5.5, 2.75, and 3.83 GeV per nucleon [22]. Monte Carlo simulations support the conclusion that the signals are a consequence of a decay of unknown particles X17 and E38.

141 The MEG II (Muon Electron Gamma) experiment

142 Experiments using the ${}^7\text{Li}(p, e^+e^-){}^8\text{Be}$ reaction were carried out at the Paul Scherrer Institute with the MEG II superconducting solenoid spectrometer [23].
 143 Analysis of the data with $E_p = 1080$ keV exciting both of the resonances (beam
 144 fully stopping in the target) found no significant evidence supporting the X17
 145 hypothesis, results are shown in Figure 0.3. An upper bound (at 90% confidence)
 146 on the X17-to- γ branching ratio was set at $1.2 \cdot 10^{-5}$ for the 18.15 MeV state
 147 (larger than the ratio $5.8 \cdot 10^{-6}$ obtained by ATOMKI in 2016). Could add their
 148 90% C.L bounds figure also.
 149

150 0.2 X17 Project at IEAP CTU

151 The aim of the X17 project at the Van der Graaff facility of the Institute of
 152 Experimental and Applied Physics, Czech Technical University in Prague is to
 153 repeat the original ATOMKI experiments with ${}^7\text{Li}$ and ${}^3\text{H}$ targets using an inde-
 154 pendent e^+e^- spectrometer. In order to effectively measure the anomaly, we need
 155 to reconstruct both the energy and the angular correlation of the e^+e^- pairs. The
 156 spectrometer will use three layers of detectors to achieve this – Timepix 3 (Tpx3)
 157 silicon pixel detector and Multi-Wire Proportional Chamber (MWPC) layers for
 158 the angle reconstruction and a Time Projection Chamber (TPC) layer for the en-
 159 ergy reconstruction. The schematics of the prepared detector is in Figure 0.4
 160 Spectrometer CAD drawing (coordinates here or next chapter?). Cite some VdG
 161 paper, mention grant? Using https://cernbox.cern.ch/pdf-viewer/public/rf0oU1nqVLN3acZ/LuzH_submitted.pdf.
 162

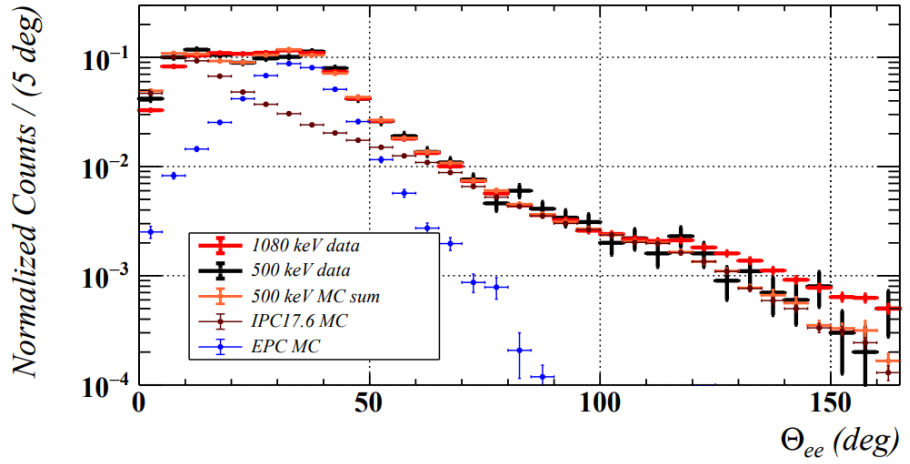


Figure 0.3: Results from the MEG II experiments – angular correlation of e^+e^- pairs with $E_{\text{sum}} \in [16, 20]$ MeV measured in the ${}^7\text{Li}(p, e^+e^-){}^8\text{Be}$ reaction with proton beam energies 500 and 1080 keV. The 500 keV dataset is fitted with Monte Carlo of both the IPC deexcitation and the EPC produced by gammas [23].

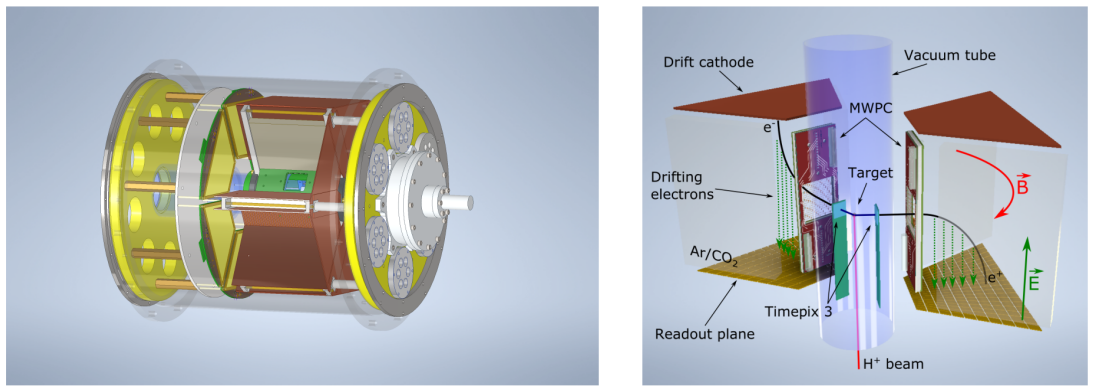


Figure 0.4: Schematics of the detector at the Van der Graaff facility at IEAP CTU.

163 The energy of e^+e^- pair produced in the reaction is given by the energy
164 available E_r in the reaction and can be distributed between them arbitrarily.
165 Nonetheless in the decay of the hypothetical X17 particle, electron and positron
166 should have similar energy and we can therefore use a disparity cut $|y| \leq 0.5$
167 for the disparity parameter (defined in Equation 0.1). Interesting events should
168 rarely have a particle with an energy below $E_r/4$ (roughly 4 MeV). Electrons with
169 such low energies are scattered significantly by even a thin layer of relatively light
170 material, for this reason the Tpx3 layer will be inside of the vacuum tube and the
171 tube will have a thinned aluminum segment or KaptonTM windows.

172 Tpx3 can measure (in each $55 \times 55 \mu\text{m}$ pixel of its 256×256 grid) time-of-arrival
173 (ToA) with 1.6 ns precision and time-over-threshold (ToT) which reflects the de-
174 posited energy. This potentially allows 3D tracking if we increase the chip thick-
175 ness at the cost of increased scattering. The layer can reconstruct the reaction
176 vertex and the angular correlation with high precision.

177 The layer of MWPCs with sensitive area $40 \times 38 \text{ mm}^2$ will be outside of
178 the beam pipe. It will provide an extra point on the particle trajectory which can
179 help with the estimation of the reaction vertex and improve the TPC performance
180 by providing its entry point.

181 The TPCs, which are a subject of this theses, are in a magnetic field of per-
182 manent magnets positioned between them and provide 3D track reconstruction
183 and subsequent momentum and particle identification (its charge, or even type
184 based on its stopping power). They avoid radiative losses thanks to the small
185 interaction with the incident particle. For the readout, triple Gas Electron Mul-
186 tiplier (GEM) will be used. The magnetic field layout in our TPCs is atypical –
187 orthogonal to the electric field inside the chamber, this is why we call them Or-
188 thogonal Fields TPC (OFTPC). Further details about our OFTPCs are provided
189 in section 1.3.

190 1. Time Projection Chamber

191 Using (2010 – a little old) <https://cds.cern.ch/record/1302071/files/CERN-PH-EP-2010-047.pdf>

193 A Time Projection Chamber (TPC) is a type of gaseous detector that uses
194 the drift in an electric field of free charges (electrons and cations, **also anions**
195 **if attachment is considered**) produced by an ionizing particle to reconstruct its
196 3D trajectory. When placed inside a magnetic field, the momentum of the incident
197 particle can be inferred from the curvature of its trajectory. Particle identification
198 is also possible using the ionization energy loss inside the TPC.

199 The original TPC used in the PEP-4 experiment at SLAC (Figure 1.1) was
200 a 2×2 m cylinder with a central cathode that produced a strong electric field,
201 making the ionization electrons drift towards one of the bases. The readout
202 consisted of MWPCs, where electrons are accelerated towards the anode wires
203 enough to further ionize the gas and cause an avalanche.

204 When a charged particle crosses the volume of a TPC, it loses energy by ex-
205 citation and ionization of the detector gas (**how much – from dE/dx + density**
206 **→ footnote?**). Most ionizing collision produce a single ionization electron, some-
207 times a few secondary electrons are produced close to the collision vertex. In
208 rare cases, the ionization electron has energy large enough to create a measurable
209 track, such an electron is called a δ -electron (**terminology, just like bellow – tech-**
210 **nically it's a (primary) ionization electron causing other (secondary) ionization**).
211 Penning transfer (collisions, light – factor 10 for gas gain in Ar/CO₂ viz PDG
212 CERN)?

213 CERES/NA45 – very inhomogeneous magnetic field

214 1.1 Charge transport in gases

215 1.1.1 Drift

216 Produced ionization electrons (**terminology – called ionization electrons in the**
217 **rest of the thesis**) are accelerated towards the readout by the electric field in-
218 side the chamber. At the same time, they lose speed by colliding with the gas
219 particles, quickly reaching a constant (for a given field \mathbf{E}, \mathbf{B}) mean drift velocity.
220 The electrons might be absorbed by electronegative impurities, such as halides
221 and oxygen.

222 In many gases (called "hot", e.g., Ar or CH₄), the drift velocity is much greater
223 than that of their thermal motion thanks to a high proportion of elastic collisions.
224 On the other hand, "cold" gases like CO₂ have a higher proportion of inelastic
225 collisions (e.g., thanks to the excitation of rotational and vibrational states) and
226 therefore much lower (**value? magnitude (implied)?**) drift velocity. (**def?**)

227 The ions produced by the ionization lose a significant portion of their energy
228 during each collision since their mass is close to the mass of the gas particles (**see**
229 **the source material – average energy loss during collision** $\Delta E = \frac{2m_i M}{(m_i + M)^2}$, **this way**
230 **it's more accurate**). This, together with their large collision cross section, makes
231 their drift velocity much smaller and their energy is close to thermal. Since their
232 momenta aren't randomized to such an extent during collisions, their diffusion

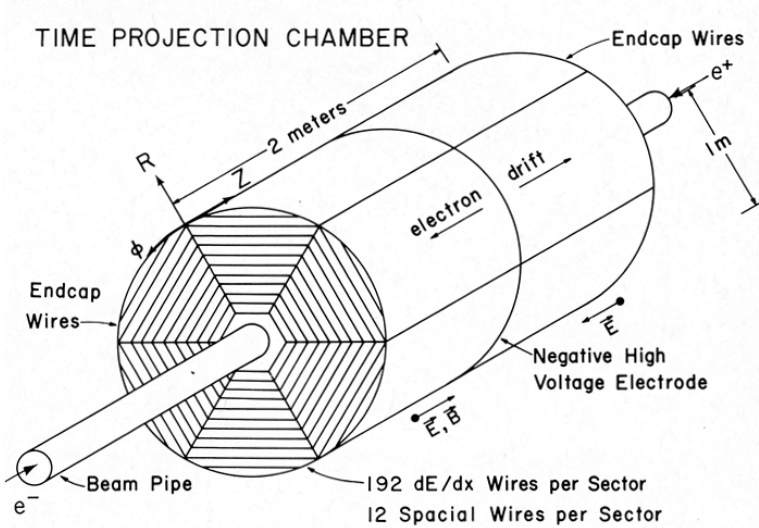


Figure 1.1: Schematic view of the PEP-4 TPC [24].

233 is smaller (more in the sense of distribution of positions, could move this to the
234 diffusion subsection).

235 The drift is also influenced by the magnetic field. Langevin derived a good
236 approximation for the drift velocity vector:

$$\mathbf{v}_d = \left(\frac{\mathbf{E}}{\|\mathbf{E}\|} + \omega\tau \frac{\mathbf{E} \times \mathbf{B}}{\|\mathbf{E}\| \|\mathbf{B}\|} + \omega^2\tau^2 \frac{\mathbf{E} \cdot \mathbf{B}}{\|\mathbf{E}\| \|\mathbf{B}\|} \cdot \frac{\mathbf{B}}{\|\mathbf{B}\|} \right) \frac{q\tau}{m(1 + \omega^2\tau^2)} \|\mathbf{E}\|, \quad (1.1)$$

237 where q is the charge of the particle, m is its mass, τ is the mean time between
238 collisions and $\omega = \frac{q}{m} \|\mathbf{B}\|$ is the Larmor frequency. In a standard TPC, \mathbf{E} is
239 nearly parallel to \mathbf{B} and the influence of the magnetic field on the drift is minimal.
240 The drift of ions is only negligibly influenced by the magnetic field ($\omega\tau \sim 10^{-4}$
241 is small due to the low drift velocity – better because it takes τ into account
242 and differs only by E/B ratio). Lorentz angle for orthogonal fields $\tan \psi = -\omega\tau$
243 (deviation from electric field) – maybe mention in the OFTPC section. Without
244 magnetic field, we can write

$$\mathbf{v}_d = \frac{q\tau}{m} \mathbf{E} = \mu \mathbf{E}, \quad (1.2)$$

245 where μ is called charge mobility.

246 1.1.2 Diffusion

247 Due to collisions a cloud of electrons or ions originating from the same point will
248 show a Gaussian density distribution at time t while drifting in the electric field
249 $\mathbf{E} = (0, 0, E_z)$:

$$\rho(x, y, z, t) = (4\pi Dt)^{-\frac{3}{2}} \exp \left(-\frac{x^2 + y^2 + (z - v_d t)^2}{4Dt} \right), \quad (1.3)$$

250 where the diffusion coefficient D can be expressed as

$$D = \frac{\lambda^2}{3\tau} = \frac{\lambda v_d}{3} = \frac{v_d^2 \tau}{3} = \frac{2\varepsilon\tau}{3m}, \quad (1.4)$$

251 where λ is the mean free path and ε the mean energy. The lateral diffusion width
252 σ_x after a drift distance L can be expressed as

$$\sigma_x^2 = 2Dt = \frac{4\varepsilon L}{3qE}. \quad (1.5)$$

253 The minimal diffusion width is given by the lowest possible energy of the particles
254 $\varepsilon_{\text{th}} = \frac{3}{2}kT$ (corresponding to thermal motion):

$$\sigma_{x,\min}^2 = \frac{2kTL}{qE}. \quad (1.6)$$

255 For electrons in "cold gases" (e.g., Ar/CO₂ mixture), the diffusion approaches
256 this limit up to a certain field intensity (~ 100 V/cm at 1 atm pressure)¹. In
257 reality, the transversal diffusion of electrons can differ significantly from their
258 longitudinal diffusion and simulations are necessary to get a precise result.

259 In most TPCs, the transversal (but not the longitudinal) diffusion is reduced
260 by the magnetic field, since it is parallel to the electric field and curves the dif-
261 fusing electrons around their mean trajectory:

$$\frac{D_T(B)}{D_T(0)} = \frac{1}{C + \omega^2 \tau_2^2}, \quad (1.7)$$

262 where C and τ_2 are parameters dependent on the gas used. At low intensity of
263 the magnetic field, we can use an approximation $C \approx 1$ and $\tau_2 \approx \tau$.

264 1.2 Readout

265 1.2.1 Multi-Wire Proportional Chamber

266 In most (2010 – almost all) TPCs operated in experiments Multi-Wire Proportion-
267 al Chamber (MWPC) was used for the readout. The electrons enter the cham-
268 ber through a cathode grid and get accelerated in the strong electric field towards
269 the thin anode wires and create a Townsend avalanche, multiplying the signal.
270 **Alternating with field wires?** The trajectory can be reconstructed using pulses
271 from each separate wire. Segmented cathode is also often used for the readout of
272 produced cations. **Gating grid (reduction of space charge effect, blocking backflow**
273 **of ions?, closed for electrons B=0, ΔV , static mode (loss of 25% el.) x opening on**
274 **trigger)? (gas amplification > 10000 required for good SNR, 100-200 ns shaping**
275 **time), figure?**

276 1.2.2 Gas Electron Multiplier

277 The Gas Electron Multiplier (GEM) is a thin metal-coated polymer sheet with
278 a high density of small holes. The amplification is achieved by applying voltage
279 on the metal layers, creating a strong electric field inside the holes and causing
280 avalanches. Double or triple stack of GEMs is usually used to create a sufficient
281 gain. From the last foil, the electrons drift to a segmented anode where the signal
282 is read. The backflow of cations is reduced compared to MWPC. An example
283 simulation of an avalanche inside GEM is shown in Figure 1.2. **Parameters?**

¹For us 0.45 mm, quite close to the actual diffusion 0.5-0.7 mm.

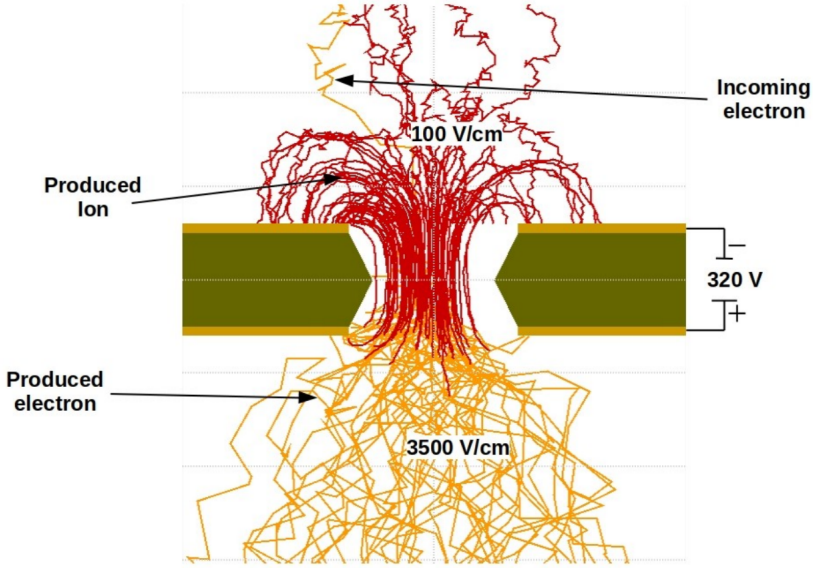


Figure 1.2: Garfield simulation of an avalanche in a GEM hole [25].

284 1.2.3 Micromegas

285 In a MICRO-MEsh GAseous Structure (Micromegas) electrons pass through a fine
 286 mesh (made out of very thin wires) into the narrow amplification gap where they
 287 are multiplied in the high field and read as signal on the segmented anode. Very
 288 high field ($30\text{-}80 \text{ kV/cm}^2$) is necessary to achieve sufficient gain. Cation backflow
 289 is heavily suppressed by the mesh.

290 1.2.4 Parallel Plate Chamber

291 ... micowell?

292 1.3 Orthogonal Fields TPC at IEAP CTU

293 At IEAP CTU, we are going to use six identical atypical TPCs with inhomogeneous
 294 toroidal magnetic field orthogonal to the electric field, hereafter referred to
 295 as Orthogonal Fields TPC (OFTPC). It has the shape of isosceles trapezoidal
 296 prism 16 centimeters high with triple-GEM readout on one of its bases. Dimen-
 297 sions of the OFTPC are discussed in detail in section 1.3.2 below. Throughout this
 298 thesis, we assume a uniform electric field along the z axis with $E_z = -400 \text{ V/cm}$.
 299 Gas mixture used in the detector (70/30) and its effect – some graph with the
 300 mixture.

301 1.3.1 Motivation and Associated Challenges

302 The reasons for the unusual field layout are mostly cost related:

- 303 • we use permanent magnets instead of a solenoid and parallel fields are
 304 difficult to accomplish this way,
- 305 • granularity of the TPC readout is limited in order to fit one SAMPA/SRS
 306 hybrid in each sector – parallel fields would bend the trajectories parallel

307 to the readout requiring more pads and different architecture.

308 In this thesis, we will show that such a setup can reach a similar energy resolution
309 as common cylindrical TPCs while reducing cost.

310 The layout introduces two complications to the track reconstruction – the
311 trajectory in inhomogeneous field is not circular and the drift is distorted by
312 the magnetic field (see Equation 1.1, in our case $\omega\tau \approx 0.08$ for 0.3 T assuming
313 $\mu \approx 0.25 \text{ T}^{-1}$, varies inside the detector). The diffusion in such setup is larger
314 since parallel orientation reduces diffusion by curling the electrons in the x - y
315 direction (see Equation 1.7) but for our relatively weak magnetic field and short
316 drift distance the difference is negligible.

317 1.3.2 Coordinate Systems and Dimensions

318 In order to describe events in our detector, we use three distinct spaces: the de-
319 tector space \mathcal{D} , the readout space \mathcal{R} and the pad space \mathcal{P} . Each space is later
320 used to represent ionization electrons at different stages of the detection process:
321 their creation in the gas, their final position when hitting the readout plane, and
322 finally their representation in the discrete pad space.

323 Detector Space

324 The detector space \mathcal{D} represents the physical space of our detector. We de-
325 scribe it using Cartesian coordinates (x, y, z) . The z -axis is the detector's axis of
326 symmetry, with its negative direction aligned with the proton beam. The origin
327 $(0, 0, 0)$ is located at the center of the irradiated target. The positive x -axis passes
328 through the center of one the OFTPCs along the intersection of its two planes
329 of symmetry. The y -axis is then chosen to maintain a right-handed coordinate
330 system.

331 Since the detector has a hexagonal symmetry, we use only one of its sectors
332 in this work – the first sector $\mathcal{D}_1 \subset \mathcal{D}$ which is defined by the condition:

$$(x, y, z) \in \mathcal{D}_1 \Leftrightarrow |y| \leq x \tan \frac{\pi}{6}. \quad (1.8)$$

333 Simulations in this sector can be applied to all sectors by rotating the coordinates
334 accordingly. The volume of the OFTPC in this sector, which has the shape of
335 a trapezoidal prism, has these boundaries:

$$x \in [x_{\min}, x_{\max}] = [6.51, 14.61] \text{ cm}, \quad (1.9)$$

$$z \in [z_{\min}, z_{\max}] = [-8, 8] \text{ cm}, \quad (1.10)$$

$$y_{\max}(x_{\min}) = -y_{\min}(x_{\min}) = 2.75 \text{ cm}, \quad (1.11)$$

$$y_{\max}(x_{\max}) = -y_{\min}(x_{\max}) = 7.45 \text{ cm}, \quad (1.12)$$

336 where $y_{\max}(x)$ is the maximal value of the y -coordinate for a given x . The read-
337 out is located at $z = 8$ cm; for some purposes, we also define the distance to
338 the readout $d_r = 8 \text{ cm} - z$ as an alternative to the z -coordinate. Keeping this
339 paragraph as it is because the OFTPC volume is distinct from the first sector
340 and some parts of this thesis use the space beyond this volume.

341 We also use spherical coordinates (r, θ, φ) with θ measured relative to the xy
342 plane.

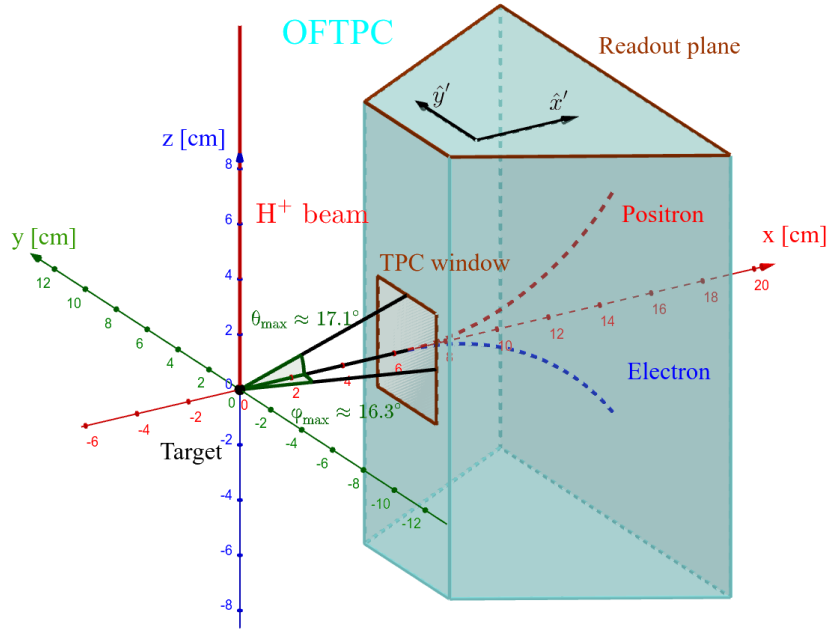


Figure 1.3: Schematics of the first sector OFTPC with detector space coordinates.

343 Readout Space

344 The readout space \mathcal{R} represents the drift time and final positions of ionization
 345 electrons as measured by an ideal continuous readout. We describe it using
 346 coordinates (x', y', t) , where x' and y' correspond to the detector coordinates at
 347 the readout plane ($z = 8$ cm). Currently not entirely sure how to put this
 348 into a figure since only x' and y' correspond to the detector coordinates, it will
 349 make more sense when visualizing the map. The drift time t is approximately
 350 proportional to d_r .

351 Pad Space

352 The pad space \mathcal{P} represents the time bin and pad number of ionization electrons
 353 as measured by an ideal discrete readout:

$$\mathcal{P} = \{(n_{\text{pad}}, n_t) \in \mathbb{N}^2 \mid n_{\text{pad}} \leq 128\}. \quad (1.13)$$

354 Technically both values can be zero as defined in the code (max channel 127).
 355 It is not really a subspace of \mathcal{R} but there is a mapping from \mathcal{R} to \mathcal{P} . It is a
 356 discretization of a part of \mathcal{R} , the mapping can be adjusted depending on the sim-
 357 ulation. If we assume uniform electric field there will be gaps, we don't use gaps
 358 in the reconstruction since the electrons should be pulled towards the pads.

359 The readout of the OFTPC will consist (is the design final?) of 128 rectangular
 360 pads arranged in a staggered pattern. Parameters of the pad layout are shown
 361 in Figure 1.4. The bottom left corner of n -th pad has coordinates $(x_{1,n}, y_{1,n})$,
 362 the top right $(x_{2,n}, y_{2,n})$ and its center has coordinates $(x_{c,n}, y_{c,n})$. The gap
 363 between neighboring pads is $g = 0.08$ cm. Time will be read out with 100 ns
 364 intervals (details?). Could also describe pad-related functions.

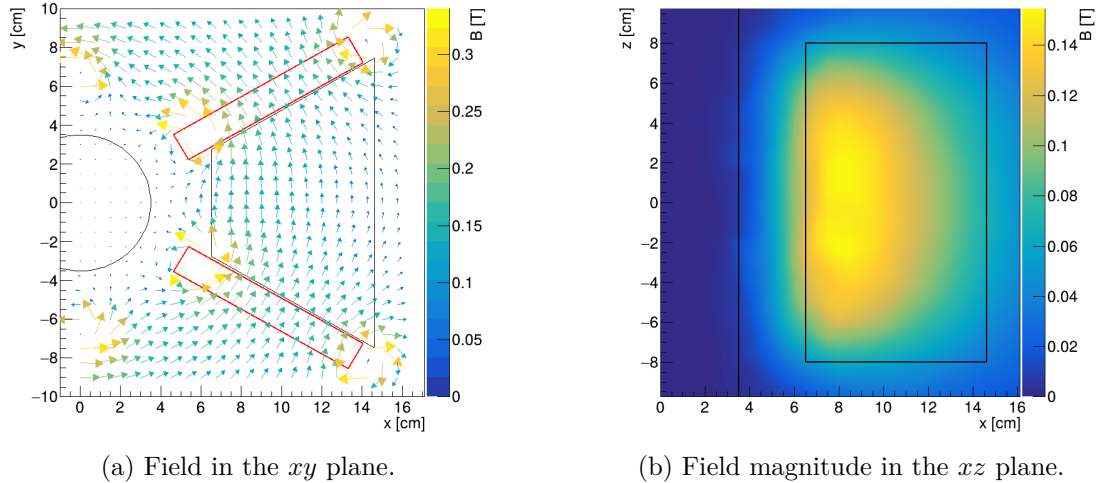


Figure 1.5: Magnetic field simulation results. The OFTPC volume and the vacuum tube are marked with black lines, the magnets are marked with red lines. The coordinates of the magnets from the CAD drawing seem to be 9/10 of the ones from the magnetic simulation (confirm and fix).

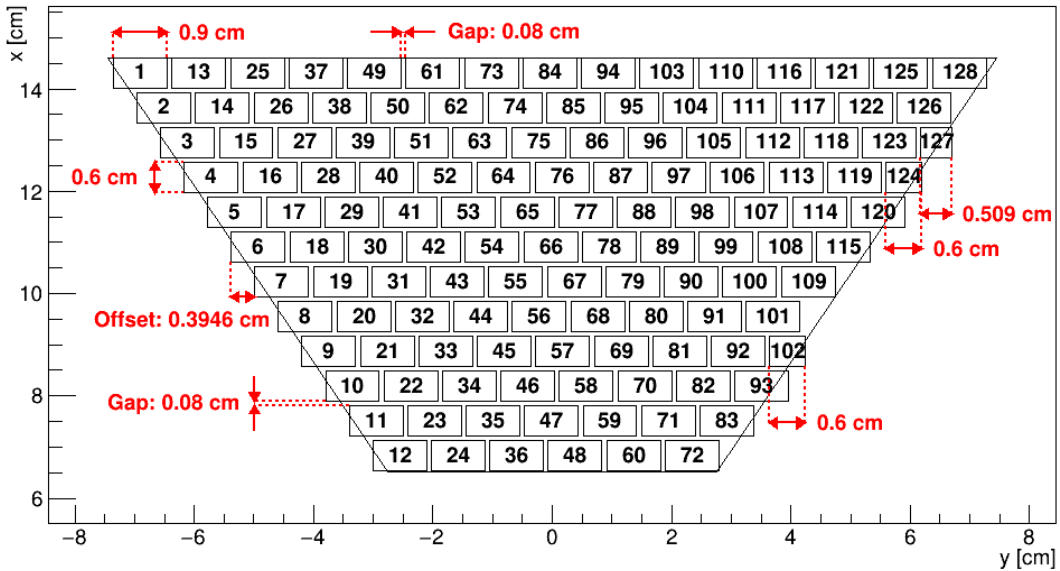


Figure 1.4: Pad layout of the OFTPC and its parameters. Pads 102, 124 and 127 are irregular, the rest has the same dimensions.

365 1.3.3 Magnetic Field Simulation

366 The magnetic field inside our detector is produced by six permanent magnets. It
 367 was simulated using Ansys Maxwell ([citation?](#)) which gives us values on a regular
 368 grid. Visualization of the magnetic field is shown in Figure 1.5. Whenever we
 369 need to work with values outside this grid, we use trilinear interpolation described
 370 below.

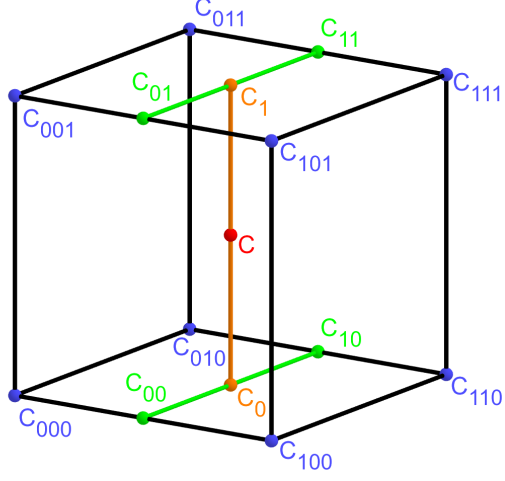


Figure 1.6: Visualization of trilinear interpolation as a composition of linear interpolations. **Image drawn in GeoGebra and inspired by a similar image on Wikipedia (which looks a bit worse) – is credit necessary?**

371 Trilinear Interpolation

372 Trilinear interpolation is a 3D generalization of linear interpolation. It can be
 373 used to interpolate a function whose values are known on a regular grid with
 374 rectangular prism cells. We use this simple method for interpolating the magnetic
 375 field, and it is later used in Section 3.2.1 to interpolate the Ionization Electron
 376 Map, a key component of our track reconstruction algorithm. In both cases, we
 377 use a regular cubic grid (apparently it is also called a [Cartesian grid](#)).

378 Could put a paragraph about linear interpolation here if it is not clear from
 379 the equations below.

380 Let us consider a cell of our regular grid (a cube) with an edge of length a
 381 containing the point $\mathbf{C} = (x, y, z)$ where we want to interpolate a function
 382 $f: \mathbb{R}^3 \rightarrow \mathbb{R}$. We know the values of this function at the vertices of the cell
 383 $\mathbf{C}_{ijk} = (x_0 + ia, y_0 + ja, z_0 + ka)$, where $i, j, k \in \{0, 1\}$ are indices. We also define
 384 the points $\mathbf{C}_{ij} = (x, y_0 + ia, z_0 + ja)$ and $\mathbf{C}_i = (x, y, z_0 + ia)$. Then the interpolated
 385 value $\hat{f}(\mathbf{C})$ can be calculated as a composition of three linear interpolations (see
 386 Figure 1.6):

$$\hat{f}(\mathbf{C}_{ij}) = (1 - x_d) f(\mathbf{C}_{0ij}) + x_d f(\mathbf{C}_{1ij}), \quad (1.14)$$

$$\hat{f}(\mathbf{C}_i) = (1 - y_d) \hat{f}(\mathbf{C}_{0i}) + y_d \hat{f}(\mathbf{C}_{1i}), \quad (1.15)$$

$$\hat{f}(\mathbf{C}) = (1 - z_d) \hat{f}(\mathbf{C}_0) + z_d \hat{f}(\mathbf{C}_1), \quad (1.16)$$

387 where x_d , y_d , and z_d are given as follows:

$$x_d = \frac{x - x_0}{a}, \quad y_d = \frac{y - y_0}{a}, \quad z_d = \frac{z - z_0}{a}. \quad (1.17)$$

388 We can also write

$$\hat{f}(\mathbf{C}) = \sum_{i,j,k \in \{0,1\}} t_x^i t_y^j t_z^k f(\mathbf{C}_{ijk}), \quad (1.18)$$

$$t_\alpha \stackrel{\text{def}}{=} \begin{pmatrix} t_\alpha^0 \\ t_\alpha^1 \end{pmatrix} = \begin{pmatrix} 1 - \alpha_d \\ \alpha_d \end{pmatrix}, \quad (1.19)$$

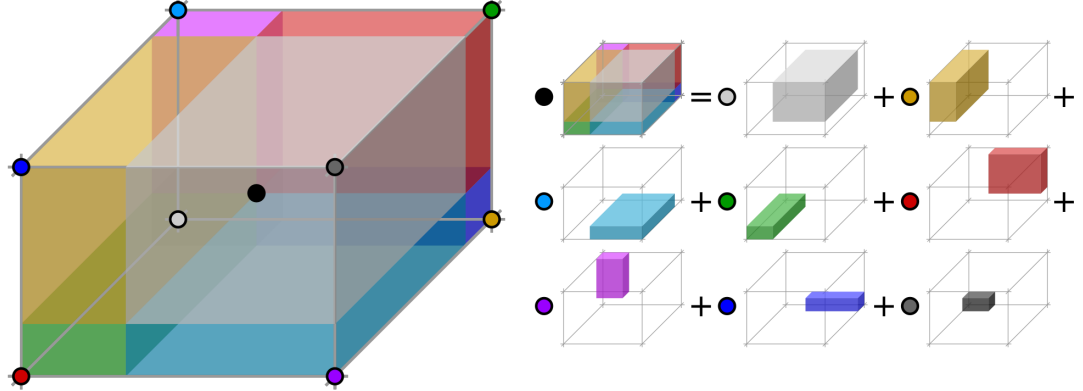


Figure 1.7: Geometric interpretation of trilinear interpolation. The colored dots represent the values in given points and the colored boxes represent the volume by which the corresponding values are multiplied. The black dot represents the interpolated value which is multiplied by the entire volume [26].

389 where $\alpha \in \{x, y, z\}$ is an index. This gives a nice geometric interpretation to the
 390 trilinear interpolation as shown in Figure 1.7. Furthermore, we can write $\hat{f}(\mathbf{C})$
 391 as a polynomial:

$$\hat{f}(\mathbf{C}) = \sum_{\alpha, \beta, \gamma \in \{0, 1\}} \sum_{i=0}^{\alpha} \sum_{j=0}^{\beta} \sum_{k=0}^{\gamma} (-1)^{(\alpha-i) + (\beta-j) + (\gamma-k)} f(\mathbf{C}_{ijk}) x_d^{\alpha} y_d^{\beta} z_d^{\gamma}. \quad (1.20)$$

392 We take advantage of this form when generalizing trilinear interpolation to irreg-
 393 ular grid in section 3.2.2.

394 Maybe a citation here, although I am not sure it is necessary since it could
 395 be considered common knowledge. The last two equations are my own. Maybe
 396 x_0 , etc. should be explicitly described.

2. Track Simulation

398 In order to develop and test the reconstruction algorithm, electron and positron
399 tracks are simulated inside the first sector \mathcal{D}_1 of our detector (see Section 1.3.2)
400 with different initial parameters. Two approaches are currently used to simulate
401 tracks, each of them for different purpose.

402 The **Microscopic Simulation** uses the Garfield++ toolkit [1]. Within this
403 toolkit, the High Energy Electro-Dynamics (HEED) program [27] is used to simu-
404 late the primary particle and the class *AvalancheMicroscopic* to simulate the drift
405 of secondary electrons created by ionization in the gas. This is the most precise
406 and time-consuming simulation used; our current goal is to be able to successfully
407 reconstruct its results and determine our best-case energy resolution.

408 The **Runge-Kutta Simulation** uses the 4th order Runge-Kutta numerical
409 integration ([add citation for Runge-Kutta](#)) to simulate the trajectory of the pri-
410 mary particle in the electromagnetic field inside the detector. It is relatively
411 fast since it does not simulate the secondary particles. It is used as part of our
412 reconstruction algorithm and for testing some parts of the reconstruction.

413 All of these simulations require the knowledge of the electromagnetic field
414 inside the detector. A uniform electric field of $400 \text{ V}\cdot\text{cm}^{-1}$ is assumed. The mag-
415 netic field was simulated in Maxwell (see Section 1.3.3). [add citation](#)

416 [Single track in positive x direction or initial parameter randomization. Im-](#)
417 [portance of gas composition, used gas compositions.](#)

418 2.1 Microscopic Simulation

419 The microscopic simulation, the most detailed simulation used in this work, is
420 performed using the Garfield++ toolkit [1].

421 The electron transport properties are simulated using the program Mag-
422 boltz ([Add citation](#)). Two different gas mixtures were used: 90% Ar + 10% CO₂
423 and 70% Ar + 30% CO₂. The second mixture will be used in our detector.
424 The temperature is set to 20 °C, the pressure is atmospheric.

425 The primary track is simulated using the program HEED [27], which is an
426 implementation of the photo-absorption ionization model. This program pro-
427 vides the parameters of ionizing collisions. HEED can also be used to simulate
428 the transport of delta electrons; we do not account for these in the current sim-
429 ulation but plan to include them in the future. The photons created in the atomic
430 relaxation cascade ([fluorescence reabsorption, ?](#)) are also not simulated.

431 Finally, we use the microscopic tracking provided by the class *AvalancheMicro-*
432 *scopic* to simulate the drift of the ionization electrons. Each electron is followed
433 from collision to collision using the equation of motion and the collision rates
434 calculated by Magboltz.

435 [First simulated track in the z direction should be described in detail here \(own](#)
436 [subsection?\). Figures.](#)

437 [Add more detailed and better description of HEED, and microscopic tracking](#)
438 [\(each their own subsection?\). Could also mention Monte Carlo \(requires gas file](#)
439 [generation - Magboltz\) and Runge-Kutta simulation implemented in Garfield,](#)

440 why we don't use them (another subsection? rename the section to Garfield++
 441 simulation and mention all relevant parts?).

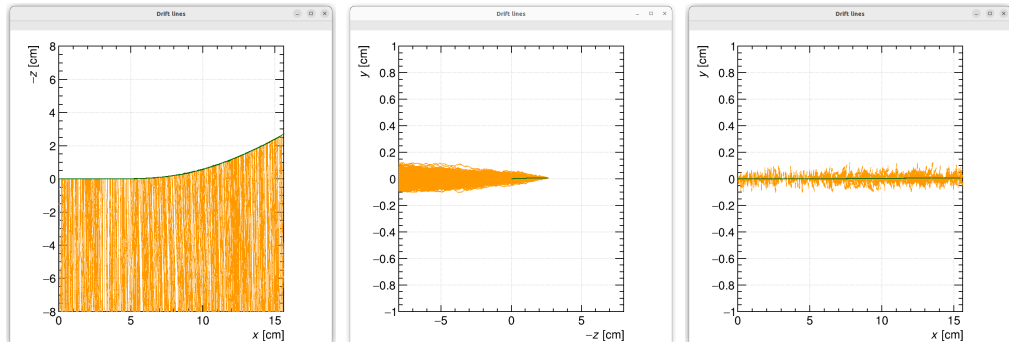


Figure 2.1: Example of a simulated electron track in 70 % argon and 30 % CO₂ atmosphere (on the left). Swap for better images, better zoom. Explain drift lines, primary particle.

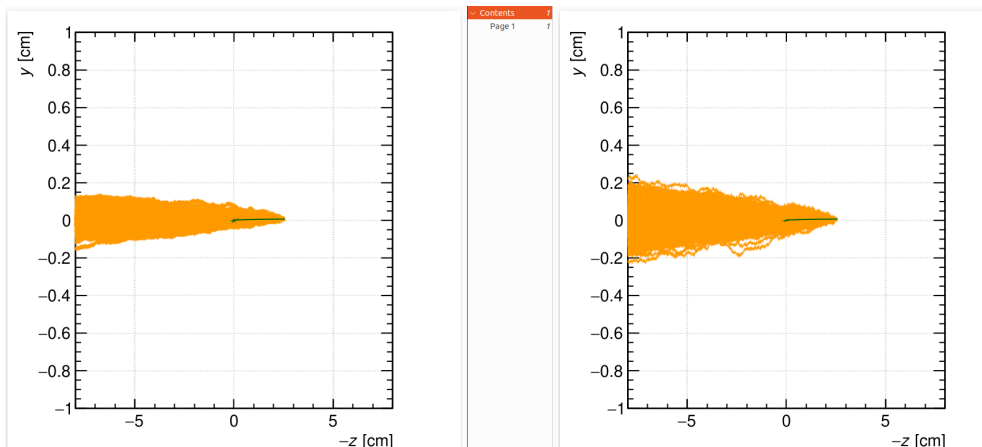


Figure 2.2: Comparison of diffusion in a simulated electron track in 70 % argon, 30 % CO₂ atmosphere and in 90 % argon, 10 % CO₂ atmosphere (on the right). Swap for better image, better zoom. Or put the same pictures for both comparisons in one subfigure, etc. Describe better.

442 2.2 Runge-Kutta Simulation

443 The Runge-Kutta simulation in this work uses the Runge-Kutta 4th order (RK4)
 444 method to numerically integrate the equation of motion of a relativistic charged
 445 particle in an electromagnetic field. Given a system of first order differential
 446 equations with an initial condition

$$\frac{dy}{dt} = \mathbf{f}(t, \mathbf{y}(t)) \quad \mathbf{y}(t_0) = \mathbf{y}_0, \quad (2.1)$$

⁴⁴⁷ we iteratively compute the estimate $\mathbf{y}_n = \mathbf{y}(t_n) = \mathbf{y}(t_0 + nh)$ as follows (citation?
⁴⁴⁸ common knowledge?):

$$\mathbf{k}_1 = \mathbf{f}(t_n, \mathbf{y}_n), \quad (2.2)$$

$$\mathbf{k}_2 = \mathbf{f}\left(t_n + \frac{h}{2}, \mathbf{y}_n + \frac{h\mathbf{k}_1}{2}\right), \quad (2.3)$$

$$\mathbf{k}_3 = \mathbf{f}\left(t_n + \frac{h}{2}, \mathbf{y}_n + \frac{h\mathbf{k}_2}{2}\right), \quad (2.4)$$

$$\mathbf{k}_4 = \mathbf{f}(t_n + h, \mathbf{y}_n + h\mathbf{k}_3), \quad (2.5)$$

⁴⁴⁹

$$\mathbf{y}_{n+1} = \mathbf{y}_n + \frac{1}{6}(\mathbf{k}_1 + 2\mathbf{k}_2 + 2\mathbf{k}_3 + \mathbf{k}_4). \quad (2.6)$$

⁴⁵⁰ Alternate forms (infinitely many) possible, accuracy vs computational cost. Runge-
⁴⁵¹ Kutta-Fehlberg with adaptive step size also possible, can potentially save some
⁴⁵² computation time especially in rapidly changing field (so maybe not in this case).

⁴⁵³ In our case, we want to integrate the equation of motion, given by the rela-
⁴⁵⁴ tivistic Lorentz force:

$$F_L^\mu = m \frac{du^\mu}{d\tau} = q F^{\mu\nu} u_\nu, \quad (2.7)$$

⁴⁵⁵ where the Einstein summation convention is used, m is the mass of the particle,
⁴⁵⁶ q is its charge, u^μ is its four-velocity, τ is the proper time (i.e., time in the particle's
⁴⁵⁷ frame of reference) and $F^{\mu\nu}$ is the electromagnetic tensor for given coordinates x^μ
⁴⁵⁸ (in our case, it is considered to be time-independent). Given the electric $\mathbf{E} =$
⁴⁵⁹ $= (E_x, E_y, E_z)$ and the magnetic field $\mathbf{B} = (B_x, B_y, B_z)$ and using the metric
⁴⁶⁰ signature $(+, -, -, -)$, the equation expands to

$$\frac{d}{d\tau} \begin{pmatrix} \gamma c \\ \gamma v_x \\ \gamma v_y \\ \gamma v_z \end{pmatrix} = \frac{q}{m} \begin{pmatrix} 0 & -\frac{E_x}{c} & -\frac{E_y}{c} & -\frac{E_z}{c} \\ \frac{E_x}{c} & 0 & -B_z & B_y \\ \frac{E_y}{c} & B_z & 0 & -B_x \\ \frac{E_z}{c} & -B_y & B_x & 0 \end{pmatrix} \begin{pmatrix} \gamma c \\ \gamma v_x \\ \gamma v_y \\ \gamma v_z \end{pmatrix}, \quad (2.8)$$

⁴⁶¹ where c is the speed of light in vacuum, $\mathbf{v} = (v_x, v_y, v_z)$ is the particle's velocity
⁴⁶² and $\gamma = (1 - \frac{v^2}{c^2})^{-\frac{1}{2}}$ is the Lorentz factor (wrong magnetic field sign in the
⁴⁶³ implementation???). Together with the equation

$$u^\mu = \begin{pmatrix} \gamma c \\ \gamma v_x \\ \gamma v_y \\ \gamma v_z \end{pmatrix} = \frac{d}{d\tau} \begin{pmatrix} ct \\ x \\ y \\ z \end{pmatrix}, \quad (2.9)$$

⁴⁶⁴ we get a system of eight first order differential equations for x^μ and u^μ , which
⁴⁶⁵ we can integrate using the Runge-Kutta method described above. As a result of
⁴⁶⁶ this integration, we get the position $\mathbf{x}(\tau_n)$, the velocity $\mathbf{v}(\tau_n)$ and the detector
⁴⁶⁷ time $t(\tau_n)$ for every proper time $\tau_n = n\tau_{\text{step}}$. Integrating using the proper time
⁴⁶⁸ means, that the step size in t gets larger by the gamma factor $\frac{dt}{d\tau} = \gamma$ (maybe
⁴⁶⁹ change it and integrate the detector time or adjust the step size accordingly). As

⁴⁷⁰ initial conditions, we use the origin of the track (x_0, y_0, z_0) , the initial velocity
⁴⁷¹ direction vector \mathbf{n} and the kinetic energy E_{kin} , we then compute γ and $\|\mathbf{v}\|$:

$$\gamma = 1 + \frac{E_{\text{kin}}}{E_0}, \quad (2.10)$$

$$\|\mathbf{v}\| = c\sqrt{1 - \gamma^{-2}}. \quad (2.11)$$

⁴⁷² Example of RK simulation – first testing track, randomized sample of 100000
⁴⁷³ tracks.

3. Track Reconstruction

In the first stage of the reconstruction algorithm, we reconstruct the track of a primary particle (either an electron or a positron). The result of this step is then used to determine the energy of the particle (Section 4).

The **Reconstruction Assuming Steady Drift** uses the standard TPC approach. With parallel fields, the drift inside a uniform electric field remains undistorted (reference to some future part of the TPC chapter). Therefore, we only need to reconstruct the z -coordinate from the drift time using the known drift velocity. We also assume that the readout coordinates (x', y', t) are known exactly, neglecting the pads and time bins.

Reconstruction using the **Ionization Electron Map** (from now on referred to as *the map*) uses a simulation of the drift of secondary (ionization) electrons within the detector volume. This simulation can then be used to interpolate the initial position of the secondary electrons. First attempts neglect the pads.

We use the map for reconstruction in two different ways. The first one uses gradient descent search along with trilinear interpolation (see Section 1.3.3) of the map. The second method uses interpolation on the irregular inverse grid with a linear polynomial.

The **Discrete Reconstruction** uses the map; instead of reconstructing the exact position of each electron, we reconstruct the center of each hit pad with the time corresponding to the midpoint of the time bin. The electron count in each TPC bin (consisting of the pad and the time bin) serves as the charge value, which is then used as a weight in the energy reconstruction fit.

3.1 Reconstruction Assuming Steady Drift

As the first step, we decided to try to reconstruct an electron track with a special set of initial parameters. The origin of the particle is given by the origin of our coordinate system. The initial direction is given by the positive x -axis. This means the magnetic field of our detector is perpendicular to the momentum of the particle at all times, and we can reduce the problem to two-dimensional space. As an example, we use a track simulated using the microscopic simulation (see Section 2.1) with a kinetic energy of 8 MeV. The gas composition used in this simulation is 90% Ar + 10% CO₂. Might be better to describe this track in Section 2.1.

In this approach to the reconstruction of the track, we decided to use the common method used in a standard TPC. This will allow us to explore the significance of the atypical behavior in our OFTPC. Additionally, we assume the readout is continuous to further simplify the problem. In this approximation, we reconstruct the initial position of each ionization electron.

The reconstruction is then defined by the following relations between the coordinates of the detector space and the readout space (see Section 1.3.2):

$$x = x', \quad (3.1)$$

$$y = y', \quad (3.2)$$

$$z = v_d t, \quad (3.3)$$

514 where v_d is the drift velocity of electrons in the given gas mixture. At a phe-
 515 nomenological level, this velocity can be considered as a function of the electric
 516 field \mathbf{E} and the magnetic field \mathbf{B} :

$$v_d = v_d(\mathbf{E}, \mathbf{B}). \quad (3.4)$$

517 Equation taken from Garfield user manual. The Garfield++ toolkit uses this
 518 fact to accelerate their drift simulation with non-microscopic approaches (could
 519 mention in the simulation chapter). Since we assume a uniform electric field in
 520 our detector and we want to neglect the effect of our unusual magnetic field, we
 521 consider the drift velocity to be constant in this scenario. We then approximate
 522 this velocity by fitting the dependence $z(t)$ taken from the simulated ionization
 523 electrons. This is in one of the provisional figures. Also, this description is
 524 not completely accurate; in reality, we fit $t1:8-y0$ with $a1*x+a0$ and then invert
 525 this and use $8-y0 = b1*t1+b0$ (old coordinates); $b1=1/a1$ functions as the drift
 526 velocity. Maybe also define this 8-z variable as an alternative to z in Section 1.3.2
 527 and then use it when correcting this.

528 Later, in a commit after this, I plotted some residues (provisional figure),
 529 which could be useful, but for some reason they are residuals from a spline fit of
 530 the track?! Probably redo this without the spline fit; just explore the difference
 531 in individual points.

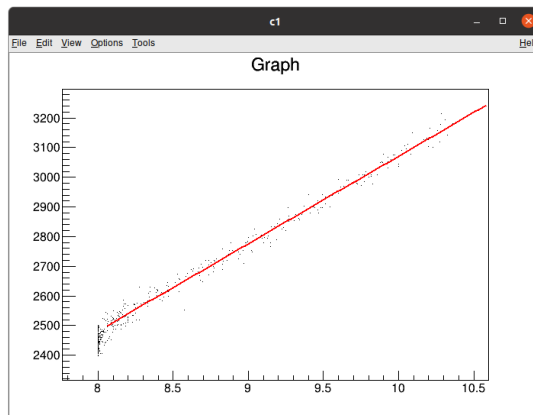


Figure 3.1: Dependence of the drift time on the z coordinate in 90 % argon and 10 % CO₂ atmosphere, fitted with a linear function. The fitted function gives us the average drift velocity in the gas and can be used for rough reconstruction in our TPC. Swap for better image with axis labels, etc. Maybe write the fitted equation.

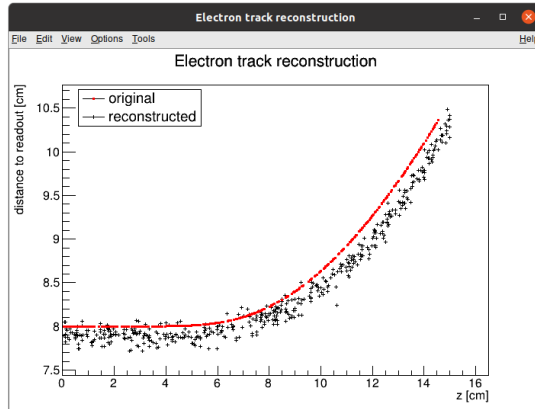


Figure 3.2: First attempt at a track reconstruction using only the drift velocity. This approach works well in a standard TPC (ideally cite some source?). 90 % argon and 10 % CO₂ atmosphere. Swap for better image, correct coordinates.

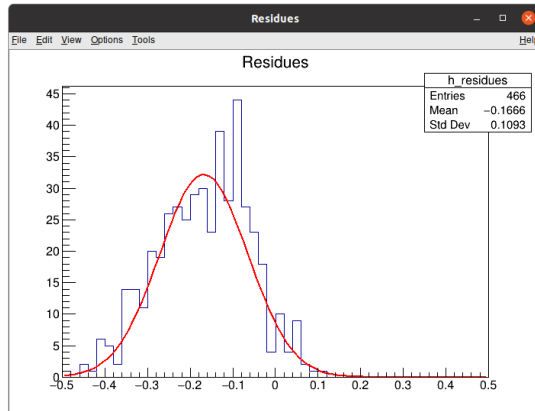


Figure 3.3: First attempt at a track reconstruction using only the drift velocity, residues. Swap for better image, correct coordinates. What's causing the shift? Explain details.

532 3.2 Ionization Electron Map

533 Inside an OFTPC, the drift of the secondary (ionization) electrons is significantly
 534 affected by its magnetic field (pictures of the distortion later, the effect is bigger
 535 for the 90/10 composition.). We need to take this into account for accurate
 536 reconstruction. In the first approximation, we assume a continuous readout (i.e.,
 537 we neglect pads). We can then reconstruct the original position of each ionization
 538 electron using its readout coordinates. For this purpose, we use the ionization
 539 electron map.

540 The ionization electron map represents a mapping from the detector space
 541 to the readout space (see Section 1.3.2). It tells us what readout coordinates
 542 (x' , y' , t) we can expect on average for an ionization electron created at the detec-
 543 tor coordinates (x , y , z). More precisely it is a mapping to the distributions on
 544 the readout space; we can simplify this as only the means $\bar{\mathcal{M}}$ and the covariance

545 matrices \mathcal{M}_{cov} , assuming Gaussian distribution.

$$\mathcal{M} : \mathcal{D} \longrightarrow \mathcal{R}, (x, y, z) \longmapsto (x', y', t). \quad (3.5)$$

546 To get an approximation of this mapping, we simulate the drift of ionization elec-
 547 trons generated on a regular grid inside the volume of our OFTPC¹. It is also
 548 useful to simulate multiple (100 in our case) electrons originating from the same
 549 position so we can get a better information about the average drift and its vari-
 550 ance. In order to get more accurate results, we use the microscopic simulation of
 551 these electrons described in Section 2.1. When evaluating the map inside the grid,
 552 we use trilinear interpolation (see Section 1.3.3). From now on, we will denote
 553 this interpolated simulation with the same symbol \mathcal{M} .

554 Finally, we need to invert the map to get the original detector coordinates
 555 (x, y, z) for the given readout coordinates (x', y', t) . In our case, we can reason-
 556 ably assume that the mapping $\overline{\mathcal{M}}$ is one-to-one (as seen in the simulations). We
 557 implemented two methods for this purpose: the gradient descent search (Sec-
 558 tion 3.2.1) and interpolation on the inverse grid (Section 3.2.2).

559 The simulation of the map is a computationally heavy task. For this reason,
 560 we use the MetaCentrum grid [3] to parallelize needed calculations. At first, this
 561 was done by evenly distributing the simulated electrons across the individual jobs
 562 in a simulation with only one electron per vertex in the regular grid with a spacing
 563 of one centimeter.

564 Later, a more efficient approach was implemented, accounting for the varying
 565 lengths of the drift of individual electrons. If we index the electrons in the order
 566 of increasing coordinates y, x, z ([picture?](#)), we can express the number n_l of full
 567 XY layers (i.e., electrons with the same z coordinate) of electrons with index less
 568 than or equal to i

$$n_l(i) = \left\lfloor \frac{i}{n_{xy}} \right\rfloor, \quad (3.6)$$

569 where n_{xy} is the number of electrons in each XY layer calculated simply by count-
 570 ing the electrons that satisfy boundary conditions for x and y . **These conditions**
 571 **should be mentioned above; sector condition + maximal x value.** The number of
 572 electrons remaining in the top layer is then

$$n_r(i) = i \bmod n_{xy}. \quad (3.7)$$

573 Finally, we can calculate the sum of the drift gaps of electrons up to index i

$$d_{\text{sum}} = (z_{\max} - z_{\min})n_{xy}n_l - \frac{n_l(n_l - 1)}{2}n_{xy}l + n_r(z_{\max} - z_{\min} - n_l l). \quad (3.8)$$

574 We then use a binary search algorithm to find the maximum index i such that
 575 the value of this sum is less than the fraction $\frac{\text{job id}}{\max \text{ job id}}$ of the total sum. This way
 576 we obtain the minimal and the maximal index of electrons simulated in the given
 577 job. **The spacing l should be probably defined above + picture of the simulating**
 578 **grid (1 layer). zmin zmax also**

579 After the simulation of the map, we calculate the mean readout coordinates
 580 assuming Gaussian distribution (i.e., we use averages). We also calculate standard

¹we do not take the detector walls into account and simulate even outside of the OFTPC which lets us interpolate even close to the walls

581 deviations in a later commit, should be upgraded to the covariance matrix. We
582 never actually plotted the distributions we get when simulating the same electron
583 multiple times, so we do not know if our assumptions are accurate (could also
584 run some statistical test to see how well the Gaussian distribution fits).

585 The obtained map is then stored in a custom class template *Field*, could
586 expand on that. Maybe earlier, since the same template is used for the magnetic
587 field.

588 Could insert a table here describing all 4 simulations of the map (gas composi-
589 tion, spacing, etc.). Simulation inside of one sector (at first double angle). Extra
590 space on the sensor. Edge cases not taken into account (TPC wall). Using qsub
591 (not sure if important). Add plots of distortion of the coordinates. Could also do
592 these plots in a different way (e.g., drawing all the endpoints of each ionization
593 electron or some error ellipse plot).

594

595 Images to add (comparison of both simulations):

- 596 • 3D visualization of the map, simulation example
- 597 • z vs. t plot
- 598 • XY plane distortion for different z values; with arrows and error bars, for
599 all z -layers with different colors
- 600 • XZ plane ($y = 0$) distortion in x (maybe not necessary?)
- 601 • XT plot ($y = 0$) showing (small) distortion in drift times

602

603 More images:

- 604 • Residuals of the continuous readout reconstruction.

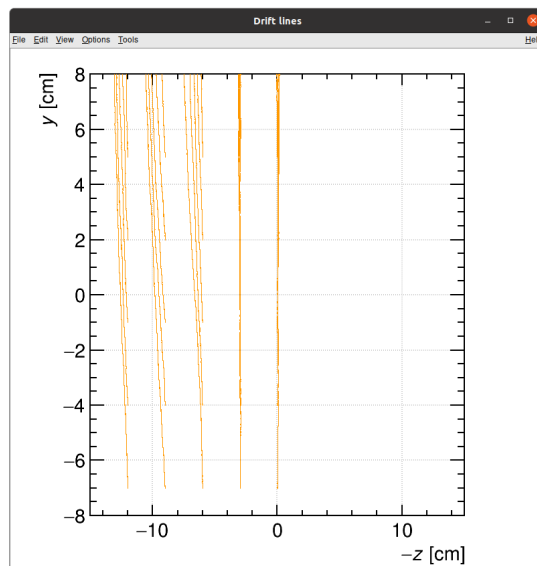


Figure 3.4: Example of map generation. Swap for better image, correct coordinates.

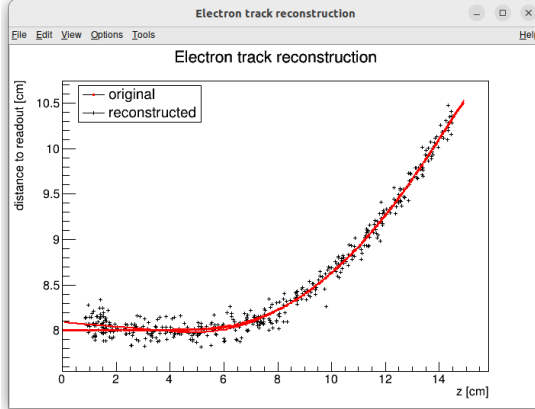


Figure 3.5: Example reconstruction with the map. Swap for better image, correct coordinates.

605 3.2.1 Gradient Descent Search

606 The first implemented method of reconstruction uses a gradient descent search
 607 to calculate an inversion of the map $\bar{\mathcal{M}}$ in a given point. Gradient descent is
 608 an iterative minimization algorithm for multivariate functions. Let $R \in \mathcal{R}$ be
 609 a point in the readout space; we want to find a point $D = (x, y, z) \in \mathcal{D}$ in
 610 the detector space such that

$$611 \quad \bar{\mathcal{M}}(D) = R = (x'_R, y'_R, t_R). \quad (3.9)$$

612 We define a function f_R in the readout space as a distance in this space:

$$613 \quad f_R(x', y', t) = \sqrt{(x' - x'_R)^2 + (y' - y'_R)^2 + v_d^2(t - t_R)^2}, \quad (3.10)$$

614 where v_d is an approximation of the drift velocity in the TPC, obtained from
 615 the reconstruction in Section 3.1 (there will be an image with the linear fit there).
 616 We make an initial guess (actually in the original code we just take $z = 0$):

$$617 \quad D_0 = (x'_R, y'_R, v_d t). \quad (3.11)$$

618 Assuming we have the n -th estimate D_n , we calculate the i -th component of
 619 the gradient of $f_R \circ \bar{\mathcal{M}}$ numerically using central differences:

$$620 \quad [\nabla(f_R \circ \bar{\mathcal{M}})]^i(D_n) \approx \frac{f_R(\bar{\mathcal{M}}(D_n + s \cdot e^i)) - f_R(\bar{\mathcal{M}}(D_n - s \cdot e^i))}{2s}, \quad (3.12)$$

621 where $e^i \in \mathcal{D}$ is the i -th coordinate vector and s is the step size. The step size
 622 should be sufficiently small; initially, we set it as a fraction of the map's grid
 623 spacing $s = \frac{l}{10}$. During the minimization, we check that $f_R(\bar{\mathcal{M}}(D_n)) < 10s$
 624 at all times. When using trilinear interpolation, it would be more efficient to
 calculate the gradient explicitly (\pm same result). This could be implemented
 inside the *Field* template class. The next iteration can be calculated as follows:

$$625 \quad D_{n+1} = D_n - \gamma \nabla(f_R \circ \bar{\mathcal{M}})(D_n), \quad (3.13)$$

626 where $\gamma \in \mathbb{R}^+$ is the damping coefficient. It should be set to a small enough
 627 value to ensure convergence, but large enough for sufficient converging speed.

625 The minimization stops either when the error $f_R(\bar{\mathcal{M}}(D_n))$ drops below a specified
 626 value or when the number of iterations exceeds a certain limit (in this case,
 627 a message is printed into the console). The parameters of this method can be
 628 further optimized (e.g., a better choice of γ , gradient computation); instead, we
 629 later decided to use the interpolation on the inverse grid described in the next
 630 section.

631 Measure reconstruction duration and compare it with the inverse grid inter-
 632 polation? Also compare the result? Not sure if this has to be cited.

633 3.2.2 Interpolation on the Inverse Grid

634 Interpolating between known points in the readout space. Gaussian elimina-
 635 tion, multivariate polynomial. Benefits compared to the gradient descent search
 636 method (one-time computation for the whole map is easy to achieve if needed).

637 The currently used baseline reconstruction method is the interpolation on
 638 the inverse grid. Rather than attempting to invert the trilinearly interpolated
 639 map as in the previous section, we take advantage of the fact that the map $\bar{\mathcal{M}}$
 640 is one-to-one (isomorphism is supposed to preserve structure, not sure how to
 641 interpret that here). Since we have simulated values of this map on a regular
 642 grid in the detector space \mathcal{D} , we also know the inverse map $\bar{\mathcal{M}}^{-1}$ on the irregular
 643 inverse grid in the readout space \mathcal{R} . To get an approximation of the inverse map
 644 in the entire readout space, we can use interpolation.

645 Since the inverse grid is irregular, trilinear interpolation cannot be applied.
 646 Given that the simulated map is dense enough to provide a good approxima-
 647 tion considering the size of our pads, we can adopt a similar approach (more
 648 complicated and computationally heavy alternative would be natural neighbor
 649 interpolation). As shown in Equation 1.20 in Section 1.3.3, trilinear interpolation
 650 can be expressed as a polynomial:

$$\hat{f}(x, y, z) = axyz + bxy + cxz + dyz + ex + fy + gz + h, \quad (3.14)$$

651 where a, b, c, d, e, f, g, h are coefficients uniquely determined by the values of
 652 the function at the vertices of the interpolation cell. We can generalize this
 653 for a function defined on an irregular grid. Given the function values at any eight
 654 points, we can write a system of eight linear equations

$$\begin{pmatrix} x_1y_1z_1 & x_1y_1 & x_1z_1 & y_1z_1 & x_1 & y_1 & z_1 & 1 \\ \vdots & \vdots \\ x_8y_8z_8 & x_8y_8 & x_8z_8 & y_8z_8 & x_8 & y_8 & z_8 & 1 \end{pmatrix} \begin{pmatrix} a \\ \vdots \\ h \end{pmatrix} = \begin{pmatrix} f(x_1, y_1, z_1) \\ \vdots \\ f(x_8, y_8, z_8) \end{pmatrix}, \quad (3.15)$$

655 which has a unique solution for the coefficients for most values of (x_n, y_n, z_n) and
 656 $f(x_n, y_n, z_n)$, where $n \in \{1, \dots, 8\}$.

657 This approach introduces a small complication: finding the correct pseudocell
 658 (i.e., the image of eight vertices forming a cubic cell in the regular grid) in
 659 the inverse grid. The eight irregularly spaced vertices of this pseudocell do not
 660 define a unique volume, so there are multiple possible ways to partition \mathcal{R} into
 661 pseudocells, with no obvious choice among them.

662 We are currently ignoring this problem and performing binary search along
 663 x, y, z (in this order). It shouldn't matter too much because the 70/30 map

664 doesn't cause such a big distortion and was even accidentally extrapolated for all
 665 z different from the central plane. Interpolation should be generally faster than
 666 the gradient descent since we don't need to iterate. We also don't need to optimize
 667 it to improve performance, if it's too slow we can even calculate the coefficients
 668 for the entire map before reconstruction.

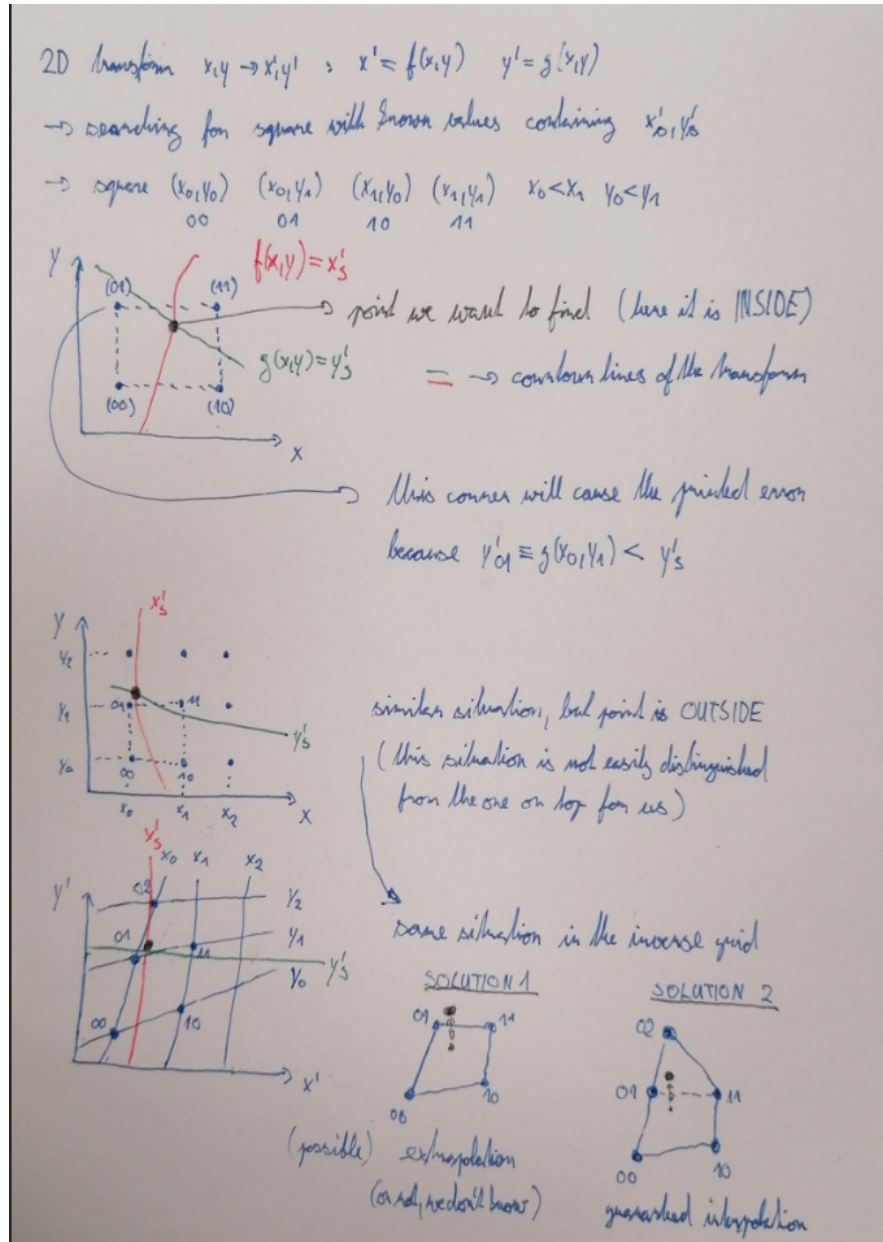


Figure 3.6: Selection of the points for interpolation. Create better images; use the explanation interpolation vs. extrapolation strange property. Solution 2 probably does not make much sense.

669 3.3 Discrete Reconstruction

670 Reconstruction with pads and time bins. Maybe testing different pads. Mapping
 671 the center of the pad (along with the midpoint of the time bin) isn't necessarily

672 the best approach since it might not correspond to the average parameters of
 673 an electron with these readout parameters (insignificant?).

674 It is also possible to make this a subsection of the map, making the previous
 675 subsections parts of a new subsection 'Map Inversion'

676 In order to get a more realistic representation of a track measured in the OFTPC,
 677 we need to take the discretization of the position and time data into account.
 678 The readout of the OFTPC will consist of 128 pads, their layout is shown in
 679 Figure 1.4. Time will be read out with $t_{\text{int}} = 100$ ns intervals.

680 As a first approximation, we can neglect the multiplication in the triple-GEM
 681 and assume an ideal charge readout. The time is started at the beginning of
 682 the electron/positron simulation (randomize this time a bit and see what it does
 683 to the reconstruction). The readout coordinates $(x', y', t) \in \mathcal{R}$ of each ionization
 684 electron can be mapped to the pad coordinates $(n_{\text{pad}}, n_t) \in \mathcal{P}$ (using the param-
 685 eters described in Section 1.3.2):

$$n_{\text{pad}} = n: (x', y') \in \left[x_{1,n} - \frac{g}{2}, x_{2,n} + \frac{g}{2} \right] \times \left[y_{1,n} - \frac{g}{2}, y_{2,n} + \frac{g}{2} \right], \quad (3.16)$$

$$n_t = \left\lceil \frac{t}{t_{\text{int}}} \right\rceil. \quad (3.17)$$

686 This way the closest pad is assigned to each readout position within the OFTPC
 687 volume². Makes sense since the pads attract the electrons, the inhomogeneity of
 688 electric field is neglected. The number of electrons in each pad (i.e., collected
 689 charge) is then counted and serves as a weight for the energy reconstruction.
 690 The reconstructed track consists of points for each $(n, n_t) \in \mathcal{P}$, we get these by
 691 reconstructing the position of a hypothetical electron with the readout coordi-
 692 nates of the pad/time bin center:

$$\mathcal{D} \ni (x, y, z) = \overline{\mathcal{M}} \left(x_{c,n}, y_{c,n}, \left(n_t - \frac{1}{2} \right) t_{\text{int}} \right). \quad (3.18)$$

²Some positions near the wall are not handled and some pads extend beyond the OFTPC volume.

693 4. Energy Reconstruction

694 The second stage is the reconstruction of the particle's energy using a fit of its
695 reconstructed track (see Section 3). We have tested three ways of reconstructing
696 the energy. Fitting is done using the MINUIT algorithm implemented in
697 ROOT [2]. **Cite some CERN article directly on MINUIT, can add a section.**

698 The **Cubic Spline Fit** is a tested and later rejected method of energy reconstruction.
699 It uses smoothly connected piecewise cubic polynomials between
700 uniformly spaced nodes. Energy is calculated using the fit parameters by computing
701 the radius of curvature in different points of the fitted curve using the known
702 magnitude of the magnetic field perpendicular to the trajectory. We rejected this
703 method because tuning of the fit to have a reasonably stable radius of curvature
704 turned out to be unpractical.

705 The **Circle and Lines Fit** was chosen as an alternative since this corresponds to the shape of a trajectory of a charged particle crossing a finite volume
706 with a homogeneous magnetic field. The energy of the particle can be estimated
707 using the fitted radius and the magnitude of the perpendicular magnetic field in
708 the middle of the TPC.

710 The **Runge-Kutta Fit** uses the 4th order Runge-Kutta numerical integration
711 described in Section 2.2. Initial parameters of the track (including the particle's
712 energy) are optimized so that the integrated trajectory fits to the reconstructed
713 one. This fit can also be performed as a single parameter (i.e., energy) fit if we
714 get the initial position and orientation of the particle on the entrance to the TPC
715 from previous detectors (Tpx3 and MWPC, see Section 0.2).

716 4.1 Cubic Spline Fit

717 The first attempt to get an early estimate of the kinetic energy of the particle
718 uses a cubic spline fit. We use an electron track starting in the origin of our
719 coordinate system with an initial direction in the positive x axis. The example
720 track is simulated microscopically (see Section 2.1) with a kinetic energy of 8 MeV
721 in a gas mixture 90% Ar + 10% CO₂ (the same track was used in Section 3.1).
722 **This track should probably be described in the simulation chapter.**

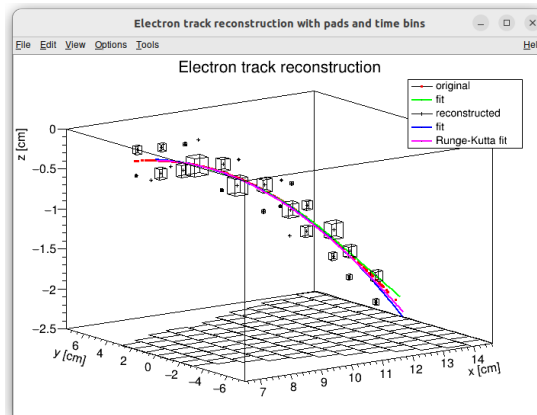


Figure 4.1: Example of a fitted reconstructed track. **Swap for better image.**

In order to calculate the spline, we use the class *TSpline3* from ROOT. This allows us to evaluate the spline using the coordinates (x_n, z_n) of each node and the derivatives d_1, d_2 in the first and the last node. We can fit these parameters of a fixed amount of nodes to the simulated trajectory. We use the IMPROVE algorithm provided by the *TMinuit* class in ROOT. This algorithm attempts to find a better local minimum after converging.

After the fit, we want to get an energy estimate. In order to calculate it, we need the radius of curvature, which we get from the fitted spline at every point of the trajectory. The part of the spline corresponding to a given node is defined as

$$z(x) = z_n + b\Delta x + c(\Delta x)^2 + d(\Delta x)^3, \quad (4.1)$$

where $\Delta x = x - x_n$ and b, c, d are coefficients. Using this equation, we derive the radius of curvature¹ as:

$$r(x) = \frac{(1 + z'^2(x))^{\frac{3}{2}}}{z''(x)} = \frac{(1 + (b + 2c\Delta x + 3d(\Delta x)^2)^2)^{\frac{3}{2}}}{2c + 6d\Delta x}. \quad (4.2)$$

Based on the geometry of the detector, we can assume the magnetic field $\mathbf{B}(x, 0, z) = (0, B(x, z), 0)$ for a track in the XZ plane. Since the electron is relativistic, the effect of the electric field on its trajectory is negligible. The Lorentz force F_L is then always perpendicular to the momentum of the electron and acts as a centripetal force F_c :

$$\mathbf{F}_L = \mathbf{F}_c, \quad (4.3)$$

$$\|e\mathbf{v} \times \mathbf{B}\| = \frac{\gamma m_e v^2}{r}, \quad (4.4)$$

$$ec\beta B = \frac{E_{0e}\beta^2}{r\sqrt{1 - \beta^2}}, \quad (4.5)$$

$$\sqrt{1 - \beta^2} = \frac{E_{0e}\beta}{ecBr}, \quad (4.6)$$

where

$$\beta^2(x) = \left[1 + \left(\frac{E_{0e}}{ecB(x, z(x))r(x)} \right)^2 \right]^{-1}, \quad (4.7)$$

where e is the elementary charge, c is the speed of light in vacuum, m_e is the rest mass of electron, $E_{0e} = m_e c^2$ is the corresponding energy, γ is the Lorentz factor, \mathbf{v} is the velocity of the electron, and $\beta = \frac{v}{c}$. We can then finally get our estimate of the kinetic energy for a given point on the trajectory as follows:

$$E_{\text{kin}}(x) = \left(\frac{1}{\sqrt{1 - \beta^2(x)}} - 1 \right) E_{0e}. \quad (4.8)$$

We can then average these estimates at multiple points to get one final estimate. This method was later rejected in favor of the circle and lines fit described in Section 4.2. **Add some figures.**

¹For the general formula see https://en.wikipedia.org/wiki/Curvature#Graph_of_a_function

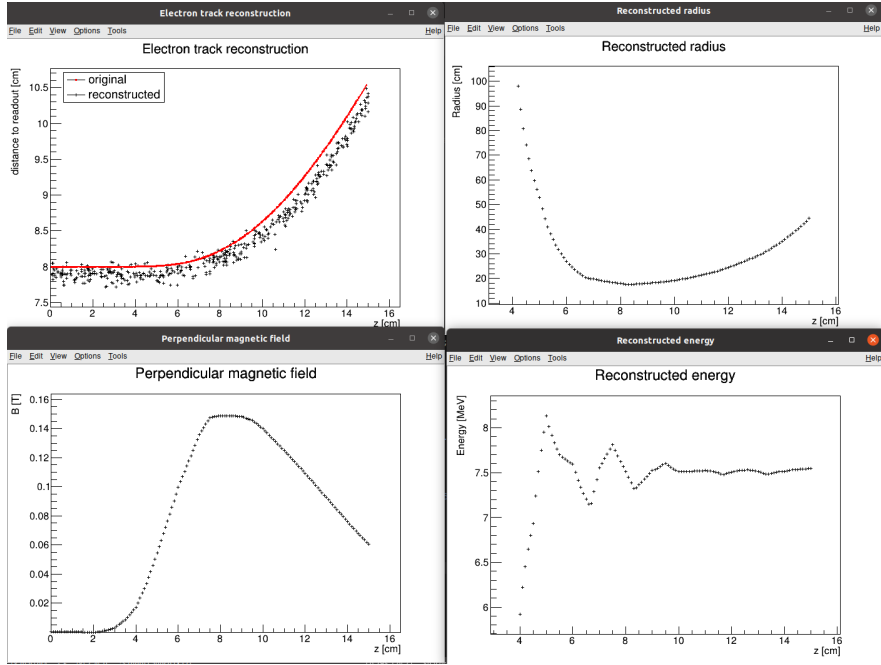


Figure 4.2: First attempt at a track reconstruction using only the drift velocity. Spline energy reconstruction attempt. Swap for better image(s) – subfigure environment, correct coordinates.

748 4.2 Circle and Lines Fit

749 Another way to estimate the particle's kinetic energy is to fit its trajectory with
 750 a circular arc with lines attached smoothly. This shape of trajectory corresponds
 751 to a movement of a charged particle through a homogeneous magnetic field per-
 752 pendicular to the particle's momentum and limited to a certain volume. In gen-
 753 eral, the shape of such a trajectory in a non-perpendicularly oriented field is
 754 a spiral. In our case, this component is negligible since the field is approxi-
 755 mately toroidal and the particle motion is nearly perpendicular to it. At first, we tested
 756 a 2D version of this fit, then we adapted it to 3D.

757 Our field is not homogeneous, it is therefore not entirely clear what value of
 758 magnetic field should be used along with the fitted radius (using equations 4.7
 759 and 4.8) to get the best estimate for the kinetic energy. Since we only use this
 760 method as the first iteration of the particle's energy that we later refine, an op-
 761 timal solution of this problem is not required. Instead, we tested two options:
 762 taking the value of the field in the middle of the fitted circular arc and taking
 763 the average field along it. We haven't really tried to plot this for multiple tracks,
 764 but these estimates are saved somewhere and could be plotted.

765 4.2.1 Two-dimensional fit

766 In the 2D case, the fitted function used for the electron track² described in Sec-
 767 tion 4.1 is defined as follows: Maybe describe this track that we used at the be-
 768 ginning somewhere earlier (section microscopic simulations → Testing track?) so
 769 that it is easier to refer to it in multiple sections. It is not part of the early GitHub

²Electron tracks bend towards negative z , we need to use the upper part of the circle

770 commits, so maybe it won't be possible to create exact replicas of the images,
 771 but they should be at least very similar.

$$z(x) = \begin{cases} a_1x + b_1 & x < x_1 \\ z_0 + \sqrt{r^2 - (x - x_0)^2} & x_1 \leq x \leq x_2, \\ a_2x + b_2 & x > x_2 \end{cases} \quad (4.9)$$

772 where $a_{1,2}$ and $b_{1,2}$ are the parameters of the lines, (x_0, z_0) is the center of the cir-
 773 cle, r is its radius, and $(x_{1,2}, z_{1,2})$ are the coordinates of the function's nodes.
 774 That means we have 9 parameters ($z_{1,2}$ are not used in the function) along with
 775 2 continuity conditions and 2 smoothness conditions. For the fit, we use the co-
 776 ordinates of the nodes and the radius of the circle, which gives us 5 independent
 777 parameters (only the radius has to be larger than half of the distance between
 778 nodes). The continuity conditions (combined with the relations for $z_{1,2}$) are as
 779 follows:

$$z_{1,2} = a_{1,2}x_{1,2} + b_{1,2} = z_0 - \sqrt{r^2 - (x_{1,2} - x_0)^2}. \quad (4.10)$$

780 The smoothness conditions are as follows:

$$a_{1,2} = \frac{x_0 - x_{1,2}}{\sqrt{r^2 - (x_{1,2} - x_0)^2}}. \quad (4.11)$$

781 Equation 4.10 gives us the values of $b_{1,2}$

$$b_{1,2} = z_{1,2} - a_{1,2}x_{1,2}. \quad (4.12)$$

782 For the coordinates of the center of the circle, we can use the fact that the center
 783 has to lie on the axis of its chord. In other words, there is a value of a parameter t
 784 such that, using the parametric equation of the axis

$$\begin{pmatrix} x_0 \\ z_0 \end{pmatrix} = \begin{pmatrix} \frac{x_1+x_2}{2} \\ \frac{z_1+z_2}{2} \end{pmatrix} + t \begin{pmatrix} \frac{z_2-z_1}{2} \\ \frac{x_1-x_2}{2} \end{pmatrix}. \quad (4.13)$$

785 At the same time, the center has to be in a distance of r from the nodes:

$$(x_1 - x_0)^2 + (z_1 - z_0)^2 = r^2, \quad (4.14)$$

$$\left(\frac{x_1 - x_2}{2} + \frac{z_1 - z_2}{2} t \right)^2 + \left(\frac{z_1 - z_2}{2} + \frac{x_2 - x_1}{2} t \right)^2 = r^2, \quad (4.15)$$

$$\left(\left(\frac{x_2 - x_1}{2} \right)^2 + \left(\frac{z_2 - z_1}{2} \right)^2 \right) t^2 + \left(\frac{x_2 - x_1}{2} \right)^2 + \left(\frac{z_2 - z_1}{2} \right)^2 - r^2 = 0. \quad (4.16)$$

786 Since our electron track bends towards negative z and $x_2 > x_1$, we only care
 787 about the solution with $t > 0$

$$t = \sqrt{\frac{r^2}{\left(\frac{x_2 - x_1}{2} \right)^2 + \left(\frac{z_2 - z_1}{2} \right)^2} - 1}, \quad (4.17)$$

788

$$x_0 = \frac{x_1 + x_2}{2} + \frac{z_2 - z_1}{2} \sqrt{\frac{r^2}{\left(\frac{x_2 - x_1}{2} \right)^2 + \left(\frac{z_2 - z_1}{2} \right)^2} - 1}, \quad (4.18)$$

$$z_0 = \frac{z_1 + z_2}{2} - \frac{x_2 - x_1}{2} \sqrt{\frac{r^2}{\left(\frac{x_2 - x_1}{2} \right)^2 + \left(\frac{z_2 - z_1}{2} \right)^2} - 1}. \quad (4.19)$$

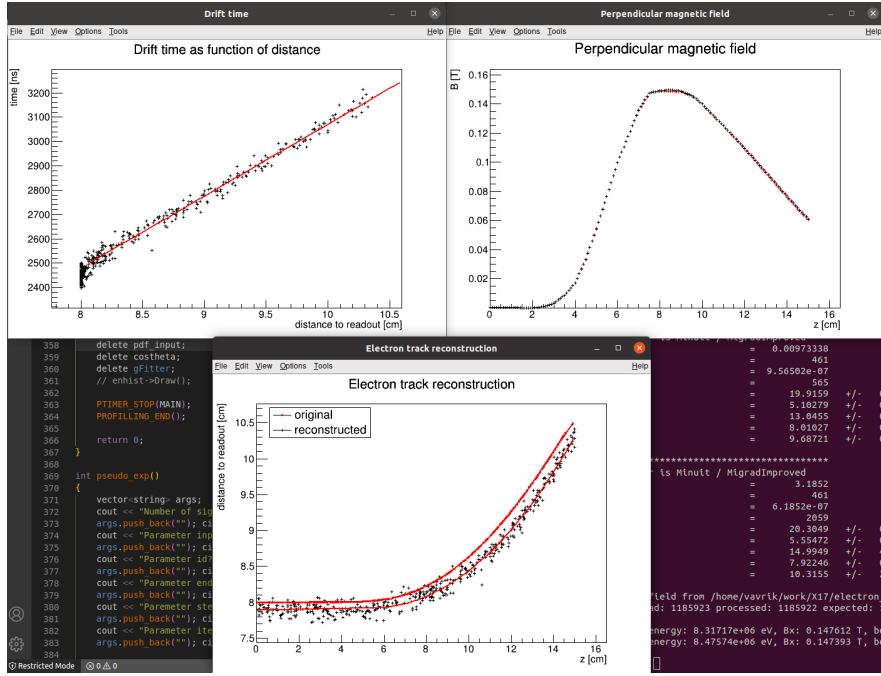


Figure 4.3: First attempt at a track reconstruction using only the drift velocity. Circle and Lines Fit in 2D. Swap for better image, correct coordinates.

789 The function defined in Equation 4.9 along with equations 4.11, 4.12, 4.18 and 4.19
 790 derived using the continuity and smoothness conditions (combined with the re-
 791 lations for $z_{1,2}$) fully define our fitted function with parameters $r, x_{1,2}, z_{1,2}$. Some
 792 pictures of the fit on the tested track. Results of the fit. Again, the actual fit
 793 uses 8-z. Use GeoGebra schematics to generate a picture of 2D geometry.

794 4.2.2 Three-dimensional fit

795 Explain the geometry and least square method used for the 3D fit. Tested on
 796 a Runge-Kutta sample, and with microscopic tracks + map simulation.

797 In three dimensions, the shape of a trajectory of a charged particle in a uniform
 798 magnetic field is a cylindrical helix. since we assume that the field is approxi-
 799 mately perpendicular to the particle's momentum at all times, we will further
 800 approximate the trajectory with a circular arc (with lines attached smoothly).

801 We assume that the initial position $\mathbf{X}_0 = (x_0, y_0, z_0)$ and direction θ, φ (spher-
 802 ical angles as in Section 1.3.2) are known, since this information will be provided
 803 by Tpx3 and MWPC layers. We could further refine it at the end of the current
 804 algorithm with some kind of global fit (all detector layers). The fit then has four
 805 free parameters (figure):

- 806 • the length of the first line l (as measured from the initial position),
- 807 • the radius of the circular arc r ,
- 808 • the central angle of the arc $\phi_{\max} \in [0, 2\pi]$,
- 809 • the direction of the curvature given by the angle $\alpha \in [0, 2\pi]$ (right-handed
 810 with respect to the particle direction, $\alpha = 0$ if the particle curves towards
 811 negative z in a plane given by \hat{z} and the direction vector).

812 Using these parameters, we can derive a parametrization of the whole curve. Let

813 \mathbf{v} be the initial unit direction vector, i.e., using the spherical angles

$$\mathbf{v} = (\cos \varphi \cos \theta, \sin \varphi \cos \theta, \sin \theta)^T, \quad (4.20)$$

814 then we can parameterize the first line as follows:

$$\mathbf{X}_{L1}(t) = \mathbf{X}_0 + t\mathbf{v} \quad t \in [0, l]. \quad (4.21)$$

815 This gives us the starting point of the arc

$$\mathbf{X}_1 = \mathbf{X}_{L1}(l) = \mathbf{X}_0 + l\mathbf{v}. \quad (4.22)$$

816 The vector $\mathbf{n} \perp \mathbf{c}_1$ that lies in the plane of curvature and points from \mathbf{X}_1 to
817 the center of curvature can be calculated using a composition of rotations. First,
818 we rotate \mathbf{v} to point in the $\hat{\mathbf{x}}$ direction, the normal for $\alpha = 0$ than points in
819 the $-\hat{\mathbf{z}}$ direction, we apply the α rotation and reverse the rotations into the $\hat{\mathbf{x}}$
820 direction:

$$\begin{aligned} \mathbf{c}_1 &= R_z(\varphi)R_y(-\theta)R_x(\alpha)R_y\left(\frac{\pi}{2}\right)R_y(\theta)R_z(-\varphi)\mathbf{v}, \\ &= R_z(\varphi)R_y(-\theta)R_x(\alpha)(-\hat{\mathbf{z}}), \\ &= \begin{pmatrix} \cos \varphi & -\sin \varphi & 0 \\ \sin \varphi & \cos \varphi & 0 \\ 0 & 0 & 1 \end{pmatrix} \begin{pmatrix} \cos \theta & 0 & -\sin \theta \\ 0 & 1 & 0 \\ \sin \theta & 0 & \cos \theta \end{pmatrix} \begin{pmatrix} 1 & 0 & 0 \\ 0 & \cos \alpha & -\sin \alpha \\ 0 & \sin \alpha & \cos \alpha \end{pmatrix} \begin{pmatrix} 0 \\ 0 \\ -1 \end{pmatrix}, \quad (4.23) \\ &= \begin{pmatrix} -\sin \alpha \sin \varphi + \cos \alpha \cos \varphi \sin \theta \\ \sin \alpha \cos \varphi + \cos \alpha \sin \varphi \sin \theta \\ -\cos \alpha \cos \theta \end{pmatrix}. \end{aligned}$$

821 Seems like in this part of the code θ is actually taken from the pole. Similarly by
822 rotating $\hat{\mathbf{y}}$, we can get the normal vector $\mathbf{n} = \mathbf{v} \times \mathbf{c}_1$ perpendicular to the plane
823 of the trajectory:

$$\mathbf{n} = R_z(\varphi)R_y(-\theta)R_x(\alpha)\hat{\mathbf{y}} = \begin{pmatrix} -\cos \alpha \sin \varphi - \sin \alpha \cos \varphi \sin \theta \\ \cos \alpha \cos \varphi - \sin \alpha \sin \varphi \sin \theta \\ \sin \alpha \cos \theta \end{pmatrix}. \quad (4.24)$$

824 This allows us to express the coordinates of the center of the circular arc:

$$\mathbf{C} = \mathbf{X}_1 + r\mathbf{c}_1. \quad (4.25)$$

825 We can then get the parametrization and the endpoint of the circular arc using
826 Rodrigues' rotation formula:

$$\begin{aligned} \mathbf{c}_2 &= \mathbf{c}_1 \cos \phi_{\max} + (\mathbf{n} \times \mathbf{c}_1) \sin \phi_{\max} + \mathbf{n}(\mathbf{n} \cdot \mathbf{c}_1)(1 - \cos \phi_{\max}), \\ &= \mathbf{c}_1 \cos \phi_{\max} - \mathbf{v} \sin \phi_{\max}, \end{aligned} \quad (4.26)$$

$$\mathbf{X}_C(\phi) = \mathbf{C} - r(\mathbf{c}_1 \cos \phi - \mathbf{v} \sin \phi) \quad \phi \in [0, \phi_{\max}], \quad (4.27)$$

$$\mathbf{X}_2 = \mathbf{X}_C(\phi_{\max}) = \mathbf{C} - r\mathbf{c}_2, \quad (4.28)$$

827 and if we define the direction vector of the second line, we also get its parametriza-
828 tion

$$\mathbf{w} = \mathbf{v} \cos \phi_{\max} + (\mathbf{n} \times \mathbf{v}) \sin \phi_{\max} = \mathbf{v} \cos \phi_{\max} + \mathbf{c}_1 \sin \phi_{\max}, \quad (4.29)$$

$$\mathbf{X}_{L2}(s) = \mathbf{X}_2 + s\mathbf{w} \quad s \in [0, \infty). \quad (4.30)$$

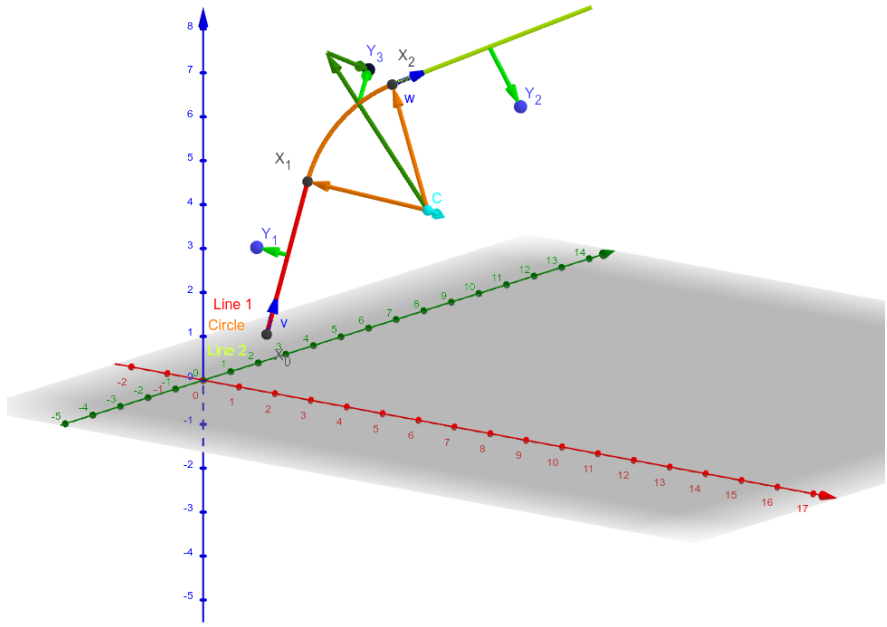


Figure 4.4: Circle and Lines Fit 3D geometry. Swap for better image.

829 The fit is performed as a (weighted) least square minimization ([MIGRAD](#)
 830 [ROOT](#)), therefore we need to derive the distance of any point \mathbf{P} to the fitted
 831 curve. For the first line, we simply compute the parameter value of the closest
 832 point on the line:

$$t_P = \mathbf{v} \cdot (\mathbf{P} - \mathbf{X}_1), \quad (4.31)$$

$$d_{P1} = \|\mathbf{P} - \mathbf{X}_{L1}(t_P)\|.$$

833 If the parameter value is outside of its bounds defined above, we take the bound-
 834 ary value instead. The distance to the second line is computed likewise. For
 835 the circular arc, we find the closest point by projecting the center connecting line
 836 onto the arc plane:

$$\mathbf{X}_{PC} = \mathbf{X}_C + r \frac{(\mathbf{P} - \mathbf{X}_C) - (\mathbf{n} \cdot (\mathbf{P} - \mathbf{X}_C))\mathbf{n}}{\|(\mathbf{P} - \mathbf{X}_C) - (\mathbf{n} \cdot (\mathbf{P} - \mathbf{X}_C))\mathbf{n}\|}, \quad (4.32)$$

$$d_{PC} = \|\mathbf{P} - \mathbf{X}_{PC}\| \quad (4.33)$$

837 Potential problem in the implementation – might not be correctly handling ϕ
 838 out of bounds, the distance could be sometimes underestimated because of this.
 839 The shortest distance out of d_{P1}, d_{PC}, d_{P2} is then taken as the distance to the curve.
 840 When calculating energy with the average field, only the arc is considered. Mid-
 841 dle field in the current implementation taken in the middle x plane (intersection
 842 with the curve). TVirtualFitter+MIGRAD, maximal num of iterations, tolera-
 843 tion. Different uncertainties in x, y, z not taken into account.

4.3 Runge-Kutta Fit

The Runge-Kutta fit uses the Runge-Kutta 4th order (RK4) numerical integration of the equation of motion (see Section 2.2) to find the best values of the track parameters – the track origin, initial velocity direction and the kinetic energy. In order to speed up the energy reconstruction, an initial guess of these parameters can be obtained from the 3D circle fit described in the previous section. Furthermore, assuming we know the track origin and orientation, we can perform a single parameter fit of the kinetic energy (**do some profiling and show that it is faster – below in the microscopic testing**).

The fit is performed as a least square minimization of the (weighted) distances of the track points (true ionization vertices from the simulation or reconstructed points). The simulated RK4 track consists of line segments with known endpoints, therefore we can calculate the distance of a point from this segment analogically to Equation 4.31 with \mathbf{v} given as a unit vector in the direction of the segment.

We need to find the segment with the lowest distance. We assume, that the distance $d_{\mathbf{P}}(\tau)$ of a point \mathbf{P} to the point on the track $\mathbf{X}(\tau)$ has a single minimum (local and global), no local maximum (except the interval endpoints) and no saddle point

$$\exists! \tau_{\min} \in [0, \tau_N]: (\forall \tau \in [0, \tau_N]: d_{\mathbf{P}}(\tau) \geq d_{\mathbf{P}}(\tau_{\min})) \vee \frac{dd_{\mathbf{P}}}{d\tau}(\tau_{\min}) = 0, \quad (4.34)$$

where N is the number of RK4 steps. This is a reasonable assumption for a track with an approximate shape of a circular arc with a radius r , since the distance d from a point \mathbf{C} on the corresponding circle of a point \mathbf{P} offset by a from the arc plane and by b from the arc's center when projected on its plane is given by the law of cosines:

$$d^2 = a^2 + b^2 + r^2 - 2br \cos \alpha, \quad (4.35)$$

where α is the angle between points \mathbf{C} and \mathbf{P} as seen from the center of the arc (see Figure 4.5). This function is strictly convex for $\alpha \in (-\frac{\pi}{2}, \frac{\pi}{2})$ and in our case, the center of the arc lies outside of the detector and α is restricted to a small interval around zero (**especially considering that the initial guess should make the fitted trajectory reasonably close to any relevant point, in the worst-case scenario, the distance is overestimated which should keep the fit from converging to such solutions**).

In a more general case, if we consider the vector $\mathbf{a}(\tau) = \mathbf{P} - \mathbf{X}(\tau)$ whose size is $\|\mathbf{a}(\tau)\| = d_{\mathbf{P}}(\tau)$, then we get

$$2d_{\mathbf{P}} \frac{dd_{\mathbf{P}}}{d\tau} = \frac{dd_{\mathbf{P}}^2}{d\tau} = \frac{d}{d\tau} \sum_i a_i^2 = 2 \sum_i a_i \frac{da_i}{d\tau} = 2\mathbf{a} \cdot \frac{d\mathbf{a}}{d\tau} = -2\mathbf{a} \cdot \frac{d\mathbf{X}}{d\tau}, \quad (4.36)$$

therefore for the derivative of $d_{\mathbf{P}}(\tau)$ to be zero, $\mathbf{a}(\tau)$ has to be perpendicular to the tangent of the track. In 3D, for a given $\mathbf{X}(\tau)$, this condition restricts \mathbf{P} to a plane. This means that for a curving track we can find a point \mathbf{P} for any two points $\mathbf{X}(\tau), \mathbf{X}(\sigma)$ with non-parallel tangents that has $\frac{dd_{\mathbf{P}}}{d\tau}(\tau) = \frac{dd_{\mathbf{P}}}{d\tau}(\sigma) = 0$, which violates the assumption 4.34. If we have a circle-and-lines track as described in the previous sections, such a point has to lie outside of the circular sector given by the arc.

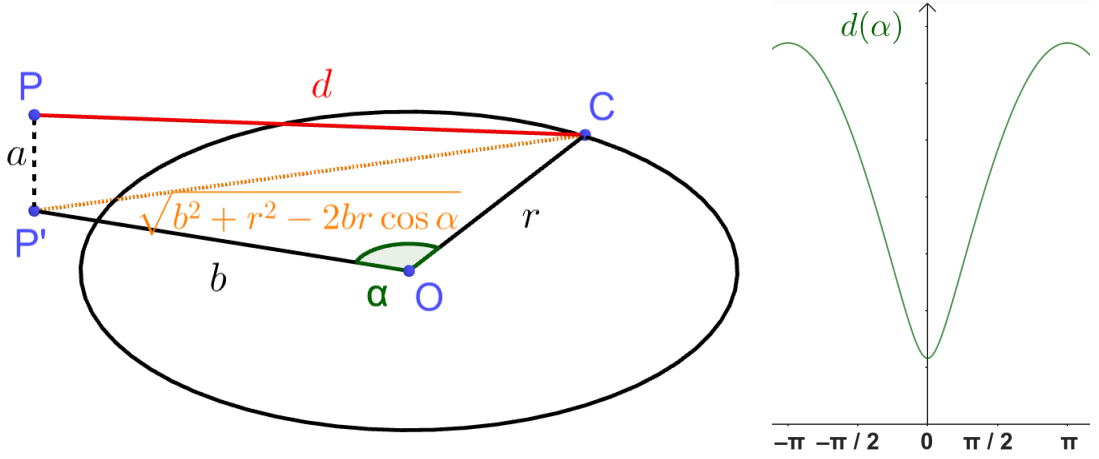


Figure 4.5: Demonstration of the convexity of the distance function $d(\alpha)$ for a circular track (see Equation 4.35).

For a planar track, the envelope of all its normals is the evolute of the curve (i.e., the set of centers of all its osculating circles). If the track has a monotonous tangent angle

$$\alpha(\tau) = \text{atan} \frac{\frac{dX_2}{d\tau}}{\frac{dX_1}{d\tau}} \quad (4.37)$$

with minimal and maximal α differing by less than π (i.e., the track changes direction by less than 180°), then all intersections of the track's normals must lie on the side of the evolute closer to the track (not obvious?, sometimes the sides are opposite?). At the same time, the intersection must lie in the half planes given by the normals at the beginning and the end of the curve and pointing away from the curve. Together, these three boundaries define a closed shape that will lie outside of the OFTPC for a typical track in our detector.

With the assumption 4.34, we can find the segment on the RK4 track with the lowest distance to a given point P using a binary search algorithm. Let the distance of the point from the n -th vertex be $d_{P,n}$. Then the difference $\Delta d_{P,n} = d_{P,n} - d_{P,n-1}$ satisfies

$$\begin{aligned} \Delta d_{P,n} &< 0 & \forall n \text{ such that } \tau_n < \tau_{\min}, \\ \Delta d_{P,n} &> 0 & \forall n \text{ such that } \tau_{n-1} > \tau_{\min}. \end{aligned} \quad (4.38)$$

Therefore, we can search for the segment containing $d_{P,\min}$ with binary search starting with $\Delta d_{P,1}$ and $\Delta d_{P,N}$, then calculate the difference $\Delta d_{P,m}$ for the middle index $m = \left\lfloor \frac{N+1}{2} \right\rfloor$. If $\Delta d_{P,m} > 0$ (minor bug in the implementation – if the value for the maximal index is negative, it shouldn't change anything), we can replace the higher index with m , otherwise we replace the lower index. The search stops when the difference between the minimal and maximal index is one. Would it be better if they were the same (maybe not)? Then the minimal value is $d_{P,n-1}$ or $d_{P,N}$ and we can take the minimum of the distances from the two segments connected to $n-1$. Currently taking the maximal index (and starting at $N-2$ maximal index $\leftrightarrow N-1$ -th point), this should be equivalent, since either $\Delta d_{P,\max} > 0$ (in the code is equivalent to max-1 here) or we are at $N-1$. The minimum of the two distances still taken.

Same details with MIGRAD etc. as previously.

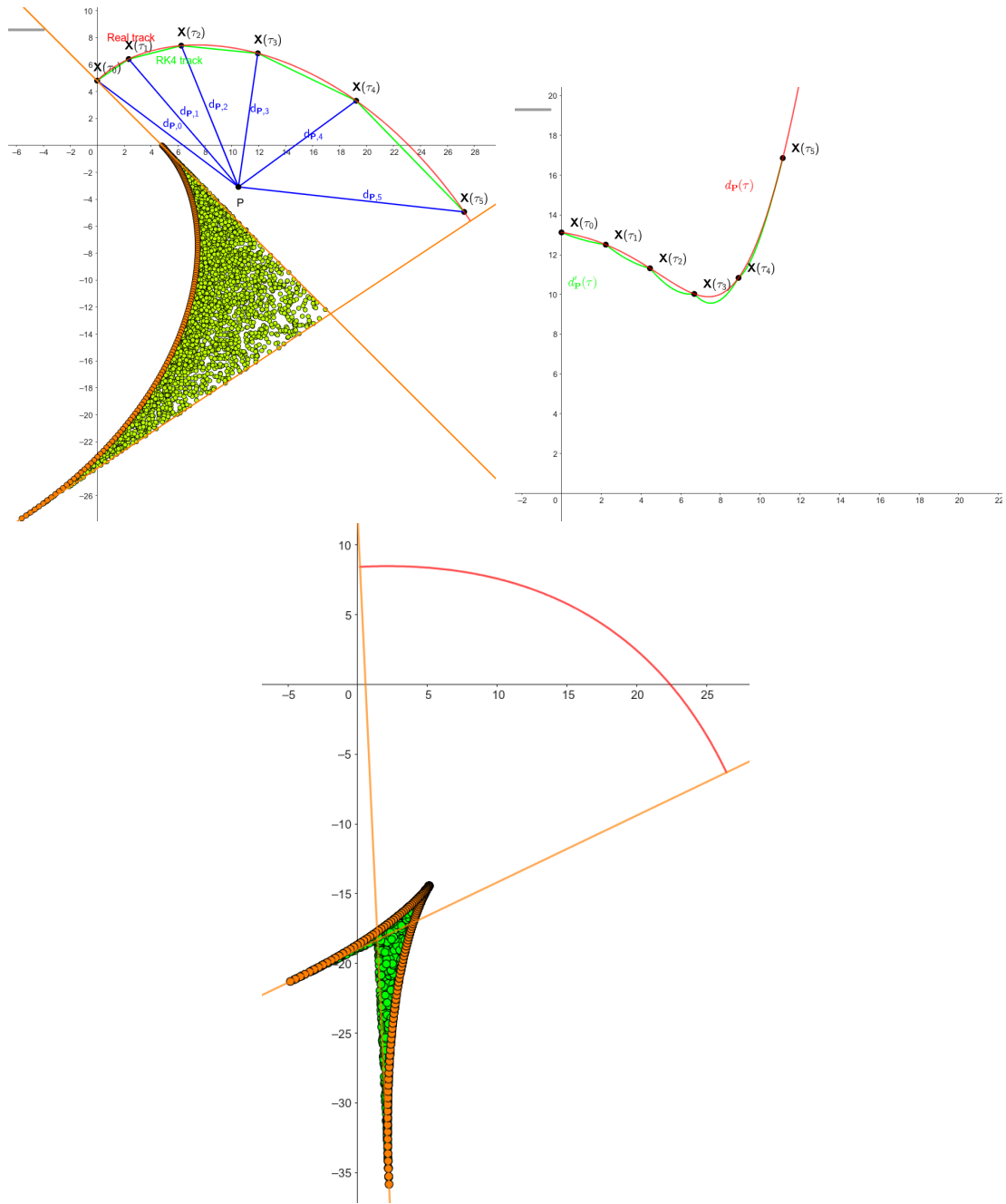


Figure 4.6: some provisional figures

Conclusion

911 Here or at the end of each section. Something about the future of this work?

912 Notes

913 General notes about the thesis:

- 914 • Check that all of the classes and other code are marked the same way in
915 the text. I used italics somewhere, could use different font for this instead.
- 916 • Check unbreakable space in front of articles. Remove excessive article usage
917 with proper nouns.
- 918 • Currently using margins for single-sided printing (bigger on the left side).
- 919 • Check that present tense is used
- 920 • Active vs passive voice usage
- 921 • American English quotation marks (") instead of British English (').
- 922 • Some of the overfull hbox warnings might change if duplex printing is used
923 (they generate black rectangles on the edge of the page), leaving them be
924 for now
- 925 • Check nobreakdash usage (is it always necessary)
- 926 • Check capitalized references (e.g., Figure, Section, Equation)
- 927 • Check $\backslash(\dots\backslash)$ math mode instead of $\$...$$. (actually unlike $\backslash[\dots\backslash]$ math mode,
928 there is apparently no real benefit to this clumsy syntax)
- 929 • Use siunitx package to ensure correct formatting, physics package for deriva-
930 tives.
- 931 • Check other stuff that's written in the MFF UK template. Apparently it
932 has since been updated and there are some differences (check for them).
- 933 • Check correct subscripts in equation (italics vs no italics)
- 934 • Consistent bold marking of points/vectors
- 935 • Correct footnotes (capital letters, etc.).
- 936 • Might have to mention GeoGebra as per the non-commercial license agree-
937 ment (Made with GeoGebra®)

938 Random notes:

- 939 • Terminology consistency – ionization/primary/secondary electrons
- 940 • Consistent TPC vs OFTPC acronym usage in the text or individual chap-
941 ters.
- 942 • Only electrons that start and end in the sector closer than 0.5 cm are used
943 for reconstruction (newest version).

- Attachment, Penning transfer and secondary ionization not considered in the microscopic simulation.
- Suspicious artifacts of trilinear interpolation in Figure 1.5. **Fixed – integers instead of doubles in the implementation, influenced reconstruction SIGNIFICANTLY (but not simulation).**

949 Future

950 Things planned for the future:

- Testing the reconstruction algorithm by measuring real particles with a known energy distribution.
- The **Fast Simulation with Ionization Electron Map** is planned for the future. It will use the HEED program [27] to simulate the primary particle and the Ionization Electron Map (see Section 3.2) to simulate the drift of secondary electrons. It should be significantly faster than the Microscopic Simulation but offer comparable precision since it will rely on an already simulated drift map. (Primary track simulated in HEED. Readout parameters by interpolating the map. Diffusion from the map for randomization.)
- Account for GEM, delta electrons, ...
- Likelihood approach instead of least squares (if it improves the reconstruction significantly), we should at least use a better method than taking the center of the TPC bin.
- More detailed electric field simulation (if needed, GEM will have more complex field)

966 Likelihood - inverse map

967 If we wanted to further improve this procedure, taking into account the whole
 968 map \mathcal{M} , we could make an "inverse map" from \mathcal{R} to distributions on \mathcal{D} . We could
 969 achieve this by taking the normalized probability density of an electron with initial
 970 coordinates (x, y, z) having readout coordinates (x', y', t) . If we fix (x', y', t) , we
 971 get an unnormalized probability density $f(x, y, z) = \mathcal{M}_{(x,y,z)}(x', y', t)$ (assuming
 972 that all initial coordinates are a priori equally likely). This could potentially
 973 improve the discrete reconstruction if we take the mean value of this probability
 974 density across the pad and time bin

$$f_{\text{pad, bin}}(x, y, z) = \frac{1}{A_{\text{pad}} \Delta t_{\text{bin}}} \int_{\text{pad, bin}} \mathcal{M}_{(x,y,z)}(x', y', t) dx' dy' dt \quad (4.39)$$

975 and using it for a likelihood fit instead of using least squares. This still assumes
 976 that all initial coordinates are equally likely which is clearly not the case for
 977 a primary particle track. In the future, we could even use the fast track simulation
 978 with the map (should be possible to make around 1000 tracks per minute per core
 979 with current settings), create a big set of tracks with reasonable parameters and
 980 use these to get an approximation of the probability distribution of the detector
 981 response. Some approximations would be necessary when interpreting the data to

982 decrease the degrees of freedom of this distribution (we would have to pick a set of
983 parameters and assume that some of them are independent). This could give us
984 an idea about the best achievable resolution (how significantly will the detector
985 response differ for a given change in energy). If the difference is significant, we
986 could try to further improve the likelihood fit.

Bibliography

- [1] Garfield++. <https://garfieldpp.web.cern.ch/garfieldpp/>. Accessed: 2023-05-18.
- [2] Rene Brun and Fons Rademakers. Root — An Object Oriented Data Analysis Framework. *Nuclear Instruments and Methods in Physics Research Section A: Accelerators, Spectrometers, Detectors and Associated Equipment*, 389(1–2):81–86, Apr 1997. Proceedings AIHENP’96 Workshop, Lausanne, Sep. 1996, See also <https://root.cern/>, Paper published in the Linux Journal, Issue 51, July 1998.
- [3] About MetaCentrum. <https://metavo.metacentrum.cz/en/about/index.html>, 2023. Accessed: 2024-11-27.
- [4] M. E. Rose. Internal Pair Formation. *Phys. Rev.*, 76:678–681, Sep 1949.
- [5] R. Essig, J. A. Jaros, W. Wester, P. Hansson Adrian, S. Andreas, T. Averett, O. Baker, B. Batell, M. Battaglieri, J. Beacham, T. Beranek, J. D. Bjorken, F. Bossi, J. R. Boyce, G. D. Cates, A. Celentano, A. S. Chou, R. Cowan, F. Curciarello, H. Davoudiasl, P. deNiverville, R. De Vita, A. Denig, R. Dharmapalan, B. Dongwi, B. Döbrich, B. Echenard, D. Espriu, S. Fegan, P. Fisher, G. B. Franklin, A. Gasparian, Y. Gershtein, M. Graham, P. W. Graham, A. Haas, A. Hatzikoutelis, M. Holtrop, I. Irastorza, E. Izaguirre, J. Jaeckel, Y. Kahn, N. Kalantarians, M. Kohl, G. Krnjaic, V. Kubarovský, H-S. Lee, A. Lindner, A. Lobanov, W. J. Marciano, D. J. E. Marsh, T. Maruyama, D. McKeen, H. Merkel, K. Moffeit, P. Monaghan, G. Mueller, T. K. Nelson, G. R. Neil, M. Oriunno, Z. Pavlovic, S. K. Phillips, M. J. Pivovaroff, R. Poltis, M. Pospelov, S. Rajendran, J. Redondo, A. Ringwald, A. Ritz, J. Ruz, K. Saenboonruang, P. Schuster, M. Shinn, T. R. Slatyer, J. H. Steffen, S. Stepanyan, D. B. Tanner, J. Thaler, M. E. Tobar, N. Toro, A. Upadye, R. Van de Water, B. Vlahovic, J. K. Vogel, D. Walker, A. Weltman, B. Wojtsekhowski, S. Zhang, and K. Zioutas. Dark Sectors and New, Light, Weakly-Coupled Particles, 2013.
- [6] F.W.N. de Boer, O. Fröhlich, K.E. Stiebing, K. Bethge, H. Bokemeyer, A. Balandia, A. Buda, R. van Dantzig, Th.W. Elze, H. Folger, J. van Klinken, K.A. Müller, K. Stelzer, P. Thee, and M. Waldschmidt. A deviation in internal pair conversion. *Physics Letters B*, 388(2):235–240, 1996.
- [7] F W N de Boer, R van Dantzig, J van Klinken, K Bethge, H Bokemeyer, A Buda, K A Müller, and K E Stiebing. Excess in nuclear pairs near 9 MeV/ invariant mass. *Journal of Physics G: Nuclear and Particle Physics*, 23(11):L85, nov 1997.
- [8] F W N de Boer, K Bethge, H Bokemeyer, R van Dantzig, J van Klinken, V Mironov, K A Müller, and K E Stiebing. Further search for a neutral boson with a mass around 9 MeV/c². *Journal of Physics G: Nuclear and Particle Physics*, 27(4):L29, apr 2001.

- 1028 [9] Attila Vitéz, A. Krasznahorkay, J. Gulyas, Margit Csatlos, Lorant Csige,
 1029 Zoltan Gacsi, Barna Nyakó, F. Boer, T. Ketel, and J. Klinken. Anomalous
 1030 Internal Pair Creation in ${}^8\text{Be}$ as a Signature of the Decay of a New Particle.
 1031 *Acta Physica Polonica B - ACTA PHYS POL B*, 39:483, 02 2008.
- 1032 [10] A. Krasznahorkay, J. Gulyas, Margit Csatlos, Attila Vitéz, T. Tornyi,
 1033 L. Stuhl, Lorant Csige, Zoltan Gacsi, A. J. Krasznahorkay, M. Hunyadi,
 1034 and T.J. Ketel. Searching for a light neutral axial-vector boson in isoscalar
 1035 nuclear transitions. *Frascati Physics Series*, 56:86, 10 2012.
- 1036 [11] A. J. Krasznahorkay, M. Csatlós, L. Csige, Z. Gácsi, J. Gulyás, M. Hunyadi,
 1037 I. Kuti, B. M. Nyakó, L. Stuhl, J. Timár, T. G. Tornyi, Zs. Vajta, T. J. Ketel,
 1038 and A. Krasznahorkay. Observation of Anomalous Internal Pair Creation
 1039 in ${}^8\text{Be}$: A Possible Indication of a Light, Neutral Boson. *Physical Review
 Letters*, 116(4), January 2016.
- 1041 [12] D.R. Tilley, J.H. Kelley, J.L. Godwin, D.J. Millener, J.E. Purcell, C.G. Sheu,
 1042 and H.R. Weller. Energy levels of light nuclei $A=8,9,10$. *Nuclear Physics A*,
 1043 745(3):155–362, 2004.
- 1044 [13] N. J. Sas, A. J. Krasznahorkay, M. Csatlós, J. Gulyás, B. Kertész, A. Krasznahorkay,
 1045 J. Molnár, I. Rajta, J. Timár, I. Vajda, and M. N. Harakeh. Observation of the X17 anomaly in the ${}^7\text{Li}(p,e^+e^-){}^8\text{Be}$ direct proton-capture
 1046 reaction, 2022.
- 1048 [14] A. J. Krasznahorkay, M. Csatlós, L. Csige, J. Gulyás, A. Krasznahorkay,
 1049 B. M. Nyakó, I. Rajta, J. Timár, I. Vajda, and N. J. Sas. New anomaly
 1050 observed in ${}^4\text{He}$ supports the existence of the hypothetical X17 particle.
 1051 *Physical Review C*, 104(4), October 2021.
- 1052 [15] D.R. Tilley, H.R. Weller, and G.M. Hale. Energy levels of light nuclei $A =$
 1053 4. *Nuclear Physics A*, 541(1):1–104, 1992.
- 1054 [16] A. J. Krasznahorkay, A. Krasznahorkay, M. Begala, M. Csatlós, L. Csige,
 1055 J. Gulyás, A. Krakó, J. Timár, I. Rajta, I. Vajda, and N. J. Sas. New
 1056 anomaly observed in ${}^{12}\text{C}$ supports the existence and the vector character of
 1057 the hypothetical X17 boson. *Phys. Rev. C*, 106:L061601, Dec 2022.
- 1058 [17] F. Ajzenberg-Selove. Energy levels of light nuclei $A = 11,12$. *Nuclear Physics
 1059 A*, 506(1):1–158, 1990.
- 1060 [18] Péter Kálmán and Tamás Keszthelyi. Anomalous internal pair creation. *The
 1061 European Physical Journal A*, 56, 08 2020.
- 1062 [19] A. Aleksejevs, S. Barkanova, Yu. G. Kolomensky, and B. Sheff. A Standard
 1063 Model Explanation for the "ATOMKI Anomaly", 2021.
- 1064 [20] Jonathan L. Feng, Bartosz Fornal, Iftah Galon, Susan Gardner, Jordan
 1065 Smolinsky, Tim M. P. Tait, and Philip Tanedo. Protophobic Fifth-Force
 1066 Interpretation of the Observed Anomaly in ${}^8\text{Be}$ Nuclear Transitions. *Phys.
 1067 Rev. Lett.*, 117:071803, Aug 2016.

- 1068 [21] Tran The Anh, Tran Dinh Trong, Attila J. Krasznahorkay, Attila Krasznahorkay,
 1069 József Molnár, Zoltán Pintye, Nguyen Ai Viet, Nguyen The Nghia,
 1070 Do Thi Khanh Linh, Bui Thi Hoa, Le Xuan Chung, and Nguyen Tuan Anh.
 1071 Checking the ${}^8\text{Be}$ Anomaly with a Two-Arm Electron Positron Pair Spec-
 1072 trometer. *Universe*, 10(4):168, April 2024.
- 1073 [22] Kh. U. Abraamyan, Ch. Austin, M. I. Baznat, K. K. Gudima, M. A. Kozhin,
 1074 S. G. Reznikov, and A. S. Sorin. Observation of structures at ~ 17 and ~ 38
 1075 MeV/c 2 in the $\gamma\gamma$ invariant mass spectra in pC, dC, and dCu collisions at
 1076 p_{lab} of a few GeV/c per nucleon, 2023.
- 1077 [23] The MEG II collaboration, K. Afanaciev, A. M. Baldini, S. Ban, H. Ben-
 1078 mansour, G. Boca, P. W. Cattaneo, G. Cavoto, F. Cei, M. Chiappini,
 1079 A. Corvaglia, G. Dal Maso, A. De Bari, M. De Gerone, L. Ferrari
 1080 Barusso, M. Francesconi, L. Galli, G. Gallucci, F. Gatti, L. Gerritzen,
 1081 F. Grancagnolo, E. G. Grandoni, M. Grassi, D. N. Grigoriev, M. Hilde-
 1082 brandt, F. Ignatov, F. Ikeda, T. Iwamoto, S. Karpov, P. R. Kettle, N. Kho-
 1083 mutov, A. Kolesnikov, N. Kravchuk, V. Krylov, N. Kuchinskiy, F. Leonetti,
 1084 W. Li, V. Malyshev, A. Matsushita, M. Meucci, S. Mihara, W. Mol-
 1085 zon, T. Mori, D. Nicolò, H. Nishiguchi, A. Ochi, W. Ootani, A. Oya,
 1086 D. Palo, M. Panareo, A. Papa, V. Pettinacci, A. Popov, F. Renga, S. Ritt,
 1087 M. Rossella, A. Rozhdestvensky, S. Scarpellini, P. Schwendimann, G. Sig-
 1088 norelli, M. Takahashi, Y. Uchiyama, A. Venturini, B. Vitali, C. Voena,
 1089 K. Yamamoto, R. Yokota, and T. Yonemoto. Search for the X17 particle
 1090 in ${}^7\text{Li}(\text{p}, \text{e}^+\text{e}^-){}^8\text{Be}$ processes with the MEG II detector, 2024.
- 1091 [24] Stewart C. Loken, H. Aihara, M. Alston-Garnjost, D. H. Badtke, J. A.
 1092 Bakken, A. Barbaro-Galtieri, A. V. Barnes, B. A. Barnett, B. Blumenfeld,
 1093 A. Bross, C. D. Buchanan, W. C. Carithers, O. Chamberlain, J. Chiba, C-
 1094 Y. Chien, A. R. Clark, O. I. Dahl, C. T. Day, P. Delpierre, K. A. Derby,
 1095 P. H. Eberhard, D. L. Fancher, H. Fujii, T. Fujii, B. Gabioud, J. W. Gary,
 1096 W. Gorn, N. J. Hadley, J. M. Hauptman, B. Heck, H. Hilke, J. E. Huth,
 1097 J. Hylen, H. Iwasaki, T. Kamae, R. W. Kenney, L. T. Kerth, R. Koda, R. R.
 1098 Kofler, K. K. Kwong, J. G. Layter, C. S. Lindsey, S. C. Loken, X-Q. Lu,
 1099 G. R. Lynch, L. Madansky, R. J. Madaras, R. Majka, J. Mallet, P. S. Mar-
 1100 tin, K. Maruyama, J. N. Marx, J. A. J. Matthews, S. O. Melnikoff, W. Moses,
 1101 P. Nemethy, D. R. Nygren, P. J. Oddone, D. Park, A. Pevsner, M. Pripstein,
 1102 P. R. Robrish, M. T. Ronan, R. R. Ross, F. R. Rouse, G. Shapiro, M. D.
 1103 Shapiro, B. C. Shen, W. E. Slater, M. L. Stevenson, D. H. Stork, H. K. Ticho,
 1104 N. Toge, M. Urban, G. J. Van Dalen, R. van Tyen, H. Videau, M. Wayne,
 1105 W. A. Wenzel, R. F. vanDaalen Wetters, M. Yamauchi, M. E. Zeller, and
 1106 W-M. Zhang. Performance of the signal processing system for the time
 1107 projection chamber. *IEEE Transactions on Nuclear Science*, 30(1):162–166,
 1108 1983.
- 1109 [25] Misbah Uddin Ahmed. Simulation of the electron and ion movement through
 1110 a 4-GEM stack, 2021. Institut für Kernphysik.
- 1111 [26] Cmglee. Trilinear interpolation visualisation, 2025. Licensed under

1112 CC BY-SA 3.0 ([https://creativecommons.org/licenses/by-sa/3.0/
1113 legalcode](https://creativecommons.org/licenses/by-sa/3.0/legalcode)). Accessed: 26-March-2025.

1114 [27] I.B. Smirnov. Modeling of ionization produced by fast charged particles in
1115 gases. *Nuclear Instruments and Methods in Physics Research Section A: Ac-
1116 celerators, Spectrometers, Detectors and Associated Equipment*, 554(1):474–
1117 493, 2005.

1118 **Acknowledgments:** Computational resources were provided by the e-INFRA
1119 CZ project (ID:90254), supported by the Ministry of Education, Youth and Sports
1120 of the Czech Republic.

List of Figures

| | | | |
|------|-----|---|----|
| 1122 | 0.1 | The ATOMKI anomalous IPC measured for different nuclei. | 5 |
| 1123 | 0.2 | Results from the Hanoi spectrometer – angular e^+e^- pair correlations measured in the ${}^7\text{Li}(p, e^+e^-){}^8\text{Be}$ reaction at $E_p = 1225$ keV [21]. | 6 |
| 1124 | 0.3 | Results from the MEG II experiments – angular correlation of e^+e^- pairs with $E_{\text{sum}} \in [16, 20]$ MeV measured in the ${}^7\text{Li}(p, e^+e^-){}^8\text{Be}$ reaction with proton beam energies 500 and 1080 keV. The 500 keV dataset is fitted with Monte Carlo of both the IPC deexcitation and the EPC produced by gammas [23]. | 7 |
| 1125 | 0.4 | Schematics of the detector at the Van der Graaff facility at IEAP CTU. | 7 |
| 1131 | 1.1 | Schematic view of the PEP-4 TPC [24]. | 10 |
| 1132 | 1.2 | Garfield simulation of an avalanche in a GEM hole [25]. | 12 |
| 1133 | 1.3 | Schematics of the first sector OFTPC with detector space coordinates. | 14 |
| 1134 | 1.5 | Magnetic field simulation results. The OFTPC volume and the vacuum tube are marked with black lines, the magnets are marked with red lines. The coordinates of the magnets from the CAD drawing seem to be 9/10 of the ones from the magnetic simulation (confirm and fix). | 15 |
| 1135 | 1.4 | Pad layout of the OFTPC and its parameters. Pads 102, 124 and 127 are irregular, the rest has the same dimensions. | 15 |
| 1136 | 1.6 | Visualization of trilinear interpolation as a composition of linear interpolations. Image drawn in GeoGebra and inspired by a similar image on Wikipedia (which looks a bit worse) – is credit necessary? | 16 |
| 1137 | 1.7 | Geometric interpretation of trilinear interpolation. The colored dots represent the values in given points and the colored boxes represent the volume by which the corresponding values are multiplied. The black dot represents the interpolated value which is multiplied by the entire volume [26]. | 17 |
| 1138 | 2.1 | Example of a simulated electron track in 70 % argon and 30 % CO_2 atmosphere (on the left). Swap for better images, better zoom. Explain drift lines, primary particle. | 19 |
| 1139 | 2.2 | Comparison of diffusion in a simulated electron track in 70 % argon, 30 % CO_2 atmosphere and in 90 % argon, 10 % CO_2 atmosphere (on the right). Swap for better image, better zoom. Or put the same pictures for both comparisons in one subfigure, etc. Describe better. | 19 |
| 1140 | 3.1 | Dependence of the drift time on the z coordinate in 90 % argon and 10 % CO_2 atmosphere, fitted with a linear function. The fitted function gives us the average drift velocity in the gas and can be used for rough reconstruction in our TPC. Swap for better image with axis labels, etc. Maybe write the fitted equation. | 23 |
| 1141 | | | |
| 1142 | | | |
| 1143 | | | |
| 1144 | | | |
| 1145 | | | |
| 1146 | | | |
| 1147 | | | |
| 1148 | | | |
| 1149 | | | |
| 1150 | | | |
| 1151 | | | |
| 1152 | | | |
| 1153 | | | |
| 1154 | | | |
| 1155 | | | |
| 1156 | | | |
| 1157 | | | |
| 1158 | | | |
| 1159 | | | |
| 1160 | | | |
| 1161 | | | |
| 1162 | | | |

| | | |
|------|---|----|
| 1163 | 3.2 First attempt at a track reconstruction using only the drift velocity. This approach works well in a standard TPC (ideally cite some source?). 90 % argon and 10 % CO ₂ atmosphere. Swap for better image, correct coordinates. | 24 |
| 1167 | 3.3 First attempt at a track reconstruction using only the drift velocity, residues. Swap for better image, correct coordinates. What's causing the shift? Explain details. | 24 |
| 1170 | 3.4 Example of map generation. Swap for better image, correct coordinates. | 26 |
| 1172 | 3.5 Example reconstruction with the map. Swap for better image, correct coordinates. | 27 |
| 1174 | 3.6 Selection of the points for interpolation. Create better images; use the explanation interpolation vs. extrapolation strange property. Solution 2 probably does not make much sense. | 29 |
| 1177 | 4.1 Example of a fitted reconstructed track. Swap for better image. | 31 |
| 1178 | 4.2 First attempt at a track reconstruction using only the drift velocity. Spline energy reconstruction attempt. Swap for better image(s) – subfigure environment, correct coordinates. | 33 |
| 1181 | 4.3 First attempt at a track reconstruction using only the drift velocity. Circle and Lines Fit in 2D. Swap for better image, correct coordinates. | 35 |
| 1184 | 4.4 Circle and Lines Fit 3D geometry. Swap for better image. | 37 |
| 1185 | 4.5 Demonstration of the convexity of the distance function $d(\alpha)$ for a circular track (see Equation 4.35). | 39 |
| 1187 | 4.6 some provisional figures | 40 |

₁₁₈₈ **List of Tables**

¹¹⁸⁹ List of Abbreviations

- ¹¹⁹⁰ **GEM** Gas Electron Multiplier
- ¹¹⁹¹ **HEED** High Energy Electro-Dynamics
- ¹¹⁹² **IEAP CTU** Institute of Experimental and Applied Physics, Czech Technical
¹¹⁹³ University in Prague
- ¹¹⁹⁴ **IPC** Internal Pair Creation
- ¹¹⁹⁵ **EPC** External Pair Creation
- ¹¹⁹⁶ **Micromegas** MICRO-MEsh GAseous Structure
- ¹¹⁹⁷ **MWPC** Multi-Wire Proportional Chamber
- ¹¹⁹⁸ **OFTPC** Orthogonal Fields TPC
- ¹¹⁹⁹ **RK4** Runge-Kutta 4th order
- ¹²⁰⁰ **TPC** Time Projection Chamber
- ¹²⁰¹ **ToA** time-of-arrival
- ¹²⁰² **ToT** time-over-threshold
- ¹²⁰³ **Tpx3** Timepix 3